University of Kentucky
UKnowledge

Theses and Dissertations--Mechanical Engineering

Mechanical Engineering

2013

NEAR WALL SHEAR STRESS MODIFICATION USING AN ACTIVE PIEZOELECTRIC NANOWIRE SURFACE

Christopher R. Guskey
University of Kentucky, cguskey@gmail.com

Click here to let us know how access to this document benefits you.

Recommended Citation

Guskey, Christopher R., "NEAR WALL SHEAR STRESS MODIFICATION USING AN ACTIVE PIEZOELECTRIC NANOWIRE SURFACE" (2013). *Theses and Dissertations--Mechanical Engineering*. 27.
https://uknowledge.uky.edu/me_etds/27

This Master's Thesis is brought to you for free and open access by the Mechanical Engineering at UKnowledge. It has been accepted for inclusion in Theses and Dissertations--Mechanical Engineering by an authorized administrator of UKnowledge. For more information, please contact UKnowledge@lsv.uky.edu.

STUDENT AGREEMENT:

I represent that my thesis or dissertation and abstract are my original work. Proper attribution has been given to all outside sources. I understand that I am solely responsible for obtaining any needed copyright permissions. I have obtained and attached hereto needed written permission statements(s) from the owner(s) of each third-party copyrighted matter to be included in my work, allowing electronic distribution (if such use is not permitted by the fair use doctrine).

I hereby grant to The University of Kentucky and its agents the non-exclusive license to archive and make accessible my work in whole or in part in all forms of media, now or hereafter known. I agree that the document mentioned above may be made available immediately for worldwide access unless a preapproved embargo applies.

I retain all other ownership rights to the copyright of my work. I also retain the right to use in future works (such as articles or books) all or part of my work. I understand that I am free to register the copyright to my work.

REVIEW, APPROVAL AND ACCEPTANCE

The document mentioned above has been reviewed and accepted by the student's advisor, on behalf of the advisory committee, and by the Director of Graduate Studies (DGS), on behalf of the program; we verify that this is the final, approved version of the student's dissertation including all changes required by the advisory committee. The undersigned agree to abide by the statements above.

Christopher R. Guskey, Student

Dr. Sean Bailey, Major Professor

Dr. James McDonough, Director of Graduate Studies

NEAR WALL SHEAR STRESS MODIFICATION USING AN ACTIVE PIEZOELECTRIC NANOWIRE SURFACE

THESIS

A Thesis submitted in partial fulfillment of the
requirements for the degree of Master of Science in
Mechanical Engineering in the College of Engineering
at the University of Kentucky

By

Christopher R. Guskey

Lexington, KY

Director: Dr. Sean Bailey, Assistant Professor of Mechanical Engineering

Lexington, KY

2013

Copyright© Christopher R. Guskey 2013

ABSTRACT OF THESIS

NEAR WALL SHEAR STRESS MODIFICATION USING AN ACTIVE PIEZOELECTRIC NANOWIRE SURFACE

An experimental study was conducted to explore the possible application of dynamically actuated nanowires to effectively disturb the wall layer in fully developed, turbulent channel flow. Actuated nanowires have the potential to be used for the mixing and filtering of chemicals, enhancing convective heat transfer and reducing drag. The first experimental evidence is presented suggesting it is possible to manipulate and subsequently control turbulent flow structures with active nanowires. An array of rigid, ultra-long (40 μm) TiO_2 nanowires was fabricated and installed in the bounding wall of turbulent channel flow then oscillated using an attached piezoelectric actuator. Flow velocity and variance measurements were taken using a single sensor hot-wire with results indicating the nanowire array significantly influenced the flow by increasing the turbulent kinetic energy through the entire wall layer.

KEYWORDS: Turbulent Flow, TiO_2 Nanowire Arrays, Nanoelectromechanical Systems (NEMS), Boundary Layers, Flow Actuator

Christopher R. Guskey

7/16/2013

NEAR WALL SHEAR STRESS MODIFICATION USING AN ACTIVE PIEZOELECTRIC NANOWIRE SURFACE

By

Christopher R. Guskey

Dr. Sean C. Bailey
Director of Thesis

Dr. James M. McDonough
Director of Graduate Studies

7/16/2013

CONTENTS

List of Tables v

List of Figures vi

1 Introduction 1
1.1 Turbulence . . . 1
1.2 Turbulent Control . . . 2

2 Analytical Background 4
2.1 Turbulent Eddies . . . 4
2.2 Characterization of Turbulence . . . 5
2.3 Turbulent Wall-Bounded Flow . . . 8

3 Motivation and Relative Research 12
3.1 Oscillating Surfaces in Flows . . . 13
3.2 Actuated Surfaces in Flows . . . 15
3.3 Nanoscale Materials in Flow . . . 16

4 Experimental Facilities, Instruments, and Measurement Procedures 17
4.1 Experiment Overview . . . 17
4.2 Turbulent Flow Channel . . . 17
4.2.1 Blower and Flow Conditioner . . . 18
4.2.2 Flow Diffuser . . . 19
4.2.3 Contraction Section . . . 19
4.2.4 Working Section . . . 20
4.3 Instrumentation . . . 23
4.3.1 Pitot-Static Tube . . . 23
4.3.2 Pressure Taps . . . 23
4.3.3 Pressure Transducer . . . 25
4.3.4 Temperature Probe . . . 25
4.3.5 Piezoelectric Nanowire Arrays . . . 26
4.3.6 Function Generator . . . 27
4.3.7 Hot-Wire Probe . . . 27
4.3.8 Hot-Wire Anemometer . . . 28
4.3.9 Filter . . . 28
4.3.10 Probe Positioning . . . 28

4.3.11 Data Acquisition 30
4.3.12 Experiment Control 30
4.4 Preliminary Measurements and Method Improvements 31
4.5 Measurement Procedures and Conditions 33

5 Results and Discussion 38
5.1 Mean Velocity and Reynolds Stress Profiles 38
5.2 Frequency Spectra 41
5.3 Kinetic Energy Addition 47
5.4 Nanowire Effects 52

6 Conclusions and Future Work 55

Bibliography 57

Vita 61

LIST OF TABLES

4.1 Experimental conditions for the 6.4 mm diameter surface. 36
4.2 Experimental conditions for the 12.7 mm diameter surface. 37

LIST OF FIGURES

2.1 Typical velocity measurement in turbulent flow. 6
2.2 Mean velocity measurements shown in m/s and m (a) and using inner scaling (b). 10
2.3 Sublayers within the turbulent wall layer. 11

4.1 Turbulent channel flow facility used in this investigation.[1] 18
4.2 Diagram of instrumentation and connections used during hot-wire measurements. 24
4.3 Scanning electron microscope image of the $BaTiO_3$ nanowires.[2] . . . 26
4.4 Diagram of insert containing measuring apparatus. 30
4.5 Position error in initial measurements. 32
4.6 Diagram of hot-wire probe location relative to nanowire arrays 34
4.7 Example calibration curve from $\mathrm{Re}_\tau = 2400$. 36

5.1 Mean streamwise velocity profiles of both actuated and unactuated cases. 39
5.2 Mean Reynolds stress profiles for both actuated and unactuated cases. 40
5.3 Frequency spectra of actuated and unactuated cases:(a) and (b) at $y^+ = 15$, (c) and (d) at $y^+ = 35$. 43
5.4 The spectral analysis for the 12.7 mm surface at Re_τ=2400, (a), with a detailed view of the region indicated by the dashed box, (b). 45
5.5 Pre-multiplied frequency spectra of actuated (a) and unactuated (b) cases at $y^+ = 15$. 46
5.6 Kinetic energy added to the turbulence due to nanowire surface actuation. 48
5.7 Additional kinetic energy injected into the turbulence due to nanowire surface actuation normalized using inner scaling. 50
5.8 Frequency spectra of 12.7 mm diameter nanowire surface in comparison to bare PZT surface after nanowire abrasion (a) with corresponding pre-multiplied spectra (b). 53
5.9 Additional kinetic energy injected into the turbulence due to nanowire surface actuation in comparison to bare PZT surface action. 54

CHAPTER 1 INTRODUCTION

1.1 Turbulence

Turbulent flow is described as a type of fluid (gas or liquid) flow in which the fluid undergoes irregular fluctuations, or mixing [3]. Though simple in description, the complexity of turbulent flow has kept it at the forefront of scientific research for over a century, leading some scholars to call it the last great unsolved problem of classical physics. Much of this complexity arises from a wide range of unsteady vortices and eddy motions, spanning several orders of magnitude in scale, interacting with each other within the flow. This complexity is only intensified when one or more surfaces are introduced confining the fluid flow. However, these are the situations of most practical importance.

At its most basic, turbulent flow is characterized by the competition between viscous forces that damp velocity fluctuations and inertial forces that generate and maintain velocity fluctuations. The ratio of inertial to viscous effects is represented by the Reynolds number, $Re = UL/\nu$, where ν is the kinematic viscosity of the fluid and U and L are the characteristic velocity and length scale of the flow, respectively. At low Reynolds numbers, velocity disturbances due to inertial effects are effectively damped by the viscous effects rendering them negligible and the flow remains laminar. However as the Reynolds number increases, the inertial effects become more relevant until a point at which the viscous effects are no longer strong enough to damp out the velocity disturbances introduced into the flow. The result is flow destabilization and turbulent flow.

The most significant turbulence effects that occur when the flow interacts with a bounding surface are located only in a thin layer near the surface. Though a tiny fraction of the overall flow field, this near wall region drives the turbulent flow characteristics within the viscous boundary layer forming near surfaces, which in turn is responsible for producing for frictional drag forces on and in engineered objects such as planes, ships, and pipelines. Major oil companies state that 25-30% of total pipeline costs is required to provide the energy necessary to pump the oil through the pipeline. The US Energy Information Administration estimates that a 5% decrease in this required pumping energy would be equivalent to doubling the US wind energy production.

1.2 Turbulent Control

The ability to control and manipulate fluid flows for technological benefit has a wide range of applications in both man-made and natural systems involving fluid flow in or around them. This has led to a multi-disciplinary research effort encompassing the fields of theoretical, computational, and experimental fluid dynamics, acoustics, control theory, chemistry, biology, and mathematics. Within the field of biology, flow modification to reduce drag within human arteries could lead to a reduction in heart attacks and stroke incidents due to clotting. In chemistry, new means chemical mixing could yield new, highly efficient chemical reactions. Additionally, flow control over wind turbine blades will increase efficiency and energy production. The potential benefits are numerous and significant.

Over the past four decades considerable research has been devoted towards understanding the dynamics of turbulence and the coherent eddy structures that dominate turbulent flow. Increased understanding of the coherent structures within turbulent flow has led to the idea of trying to control turbulence by interacting with the turbulent eddies. First suggested by Liepmann (1979)[4], it may be possible to manipulate

turbulent eddies in a predetermined manner to achieve some form of control of the turbulent properties.

Recently, a new synthesis method was developed by researchers at the University of Florida to grow ultra-long vertically-aligned piezoelectric TiO2 nanowires, which remain rigid at lengths up to 40 μm. These nanowire surfaces offer great potential for manipulating the near-wall eddy structure for reducing the skin friction over a surface. The research presented in this thesis is intended as the first step towards implementing these wires for turbulent drag reduction by demonstrating the potential for nanowire surfaces to introduce perturbations into turbulence which extend throughout the boundary layer. In the following, additional analytical background and motivation is first provided as Chapters 2 and 3, followed by a description of the experiments in Chapter 4. Experimental results are then presented and discussed in Chapter 5 and the conclusions drawn from this work are presented in Chapter 6.

CHAPTER 2 ANALYTICAL BACKGROUND

2.1 Turbulent Eddies

Perhaps the most defining property of fully turbulent flow is the chaotic and highly irregular flow velocity resulting from eddy motions throughout the flow. Produced by shear stress, these turbulent eddies range in size depending on the boundary and flow conditions. For turbulent channel flow, such as that in the current study, the largest eddies scale with the thickness of the turbulent layer or channel half height, δ. Kinetic energy is extracted from the mean flow through the production of these large-scale eddies, causing them to be referred to as the energy producing eddies, and they are the eddies of greatest turbulent energy.

Through a process referred to as the energy cascade (see Luca (2003)[5] for further details), energy is passed down without significant energy loss to smaller and smaller eddies, through an inertially-driven process until reaching an intermediate scale of eddies referred to as the Taylor microscale. At smaller scales, the eddies become small enough to eliminate and convert into heat through viscous dissipation. The scale of these smallest eddies is referred to as the Kolmogorov microscale.

The ratio between the energy-containing eddy scales and the Kolmogorov scales describes the scale separation of the turbulence, and is driven by the Reynolds number of the turbulence. At small Reynolds numbers the energy-containing eddies interact with the dissipative eddies. However, at high Reynolds numbers, only the energy-containing eddies contain information about the large-scale flow geometry, as the information about the boundary conditions producing the turbulence becomes lost

through the cascade process, and there is sufficient scale separation for the small-scale eddies to become isotropic[6]. The result is an inertial subrange in which the transport of energy can be described solely by the rate of dissipation of energy through viscosity which occurs at the Kolmogorov scales.

2.2 Characterization of Turbulence

Due to the chaotic eddy production and the existence of a wide range of eddy scales, it becomes necessary to use statistical concepts in order to analyze and characterize turbulence. Turbulent eddies create fluctuations in velocity such as those seen in figure 2.1. The velocity record, $u_i(t)$, includes both a mean, $\overline{u_i}$, and turbulent component, $u_i'(t)$, where the over-bar represents a time averaged value across the time interval, T, which is much larger than any turbulent time scale. This leads to a decomposition of the flow velocity seen in eq. 2.1.

$$u_i(t) = \overline{u_i} + u_i'(t) \tag{2.1}$$

where:

Mean velocity
$$\overline{u_i} = \frac{1}{T}\int_0^T u_i(t)\,\mathrm{d}t \tag{2.2}$$

Turbulent fluctuations
$$u_i' = u_i - \overline{u_i} \tag{2.3}$$

Here, a Cartesian coordinate system is used with $x_i = [x, y, z]$ and velocity components $u_i = [u, v, w]$.

It follows by definition that the mean of the turbulent fluctuations, $\bar{u'}$, $\bar{v'}$, $\bar{w'}$ is zero. However, the covariance of the turbulent fluctuations, $\overline{u'^2}$, $\overline{v'^2}$, $\overline{w'^2}$, $\overline{u'v'}$, $\overline{u'w'}$, $\overline{v'w'}$ is not zero and the turbulent kinetic energy

$$k = \frac{1}{2}\left(\overline{u'^2} + \overline{v'^2} + \overline{w'^2}\right) \tag{2.4}$$

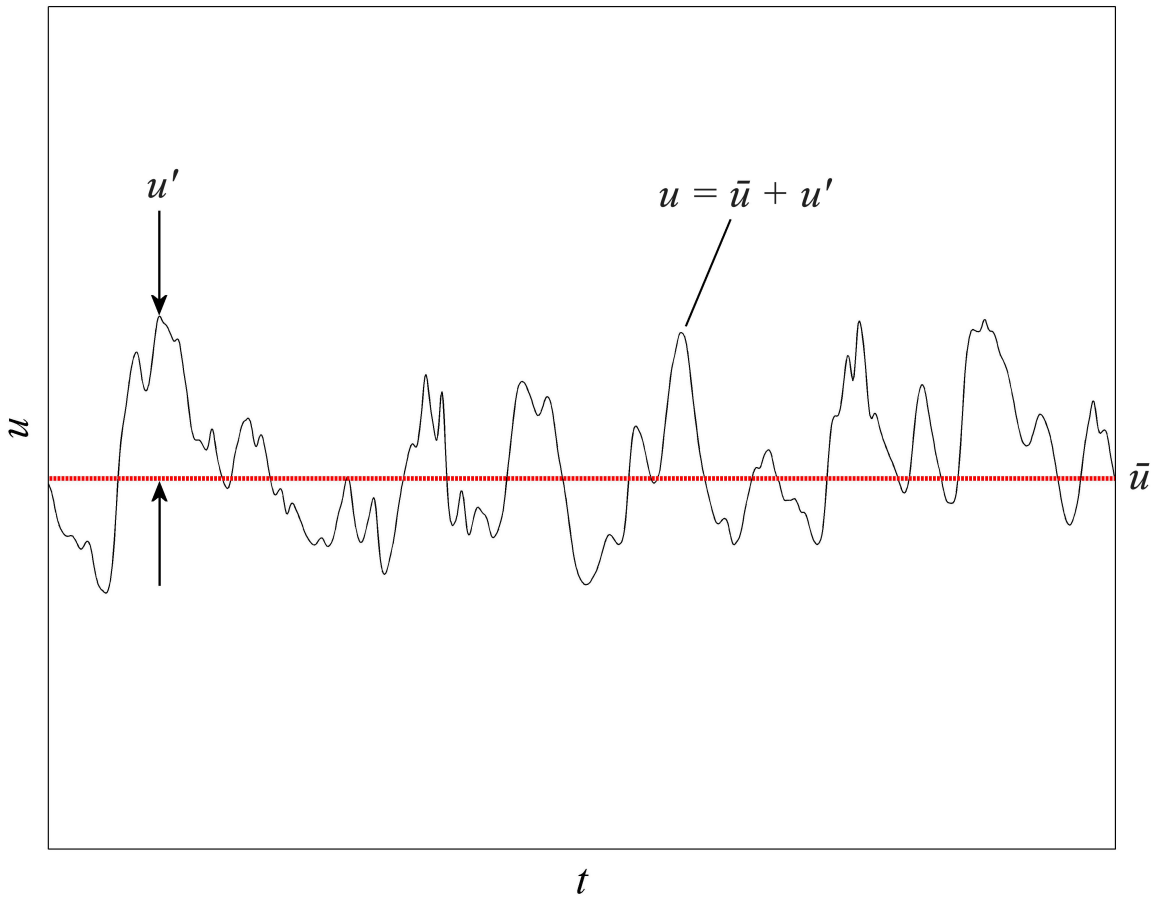

Figure 2.1: Typical velocity measurement in turbulent flow.

provides a measure of the intensity of the turbulence.

The Reynolds-averaged Navier-Stokes equations can be found by substituting eq. 2.1 into the Navier-Stokes equations and then averaging to obtain

$$\rho u_j \frac{\partial \overline{u}_i}{\partial x_j} = \rho g_i - \frac{\partial \overline{p}}{\partial x_i} + \mu \frac{\partial^2 \overline{u}_i}{\partial x_j x_j} - \frac{\partial}{\partial x_j}\left(\rho \overline{u_i' u_j'}\right) \tag{2.5}$$

for incompressible flow with only gravity, g_i as a body force. The fluid properties are the density ρ and viscosity μ. The quantity $\rho\overline{u_i' u_j'}$ is referred to as the Reynolds stress tensor, and describes how the turbulence influences the mean flow.

Here, only the streamwise component of velocity was measured, and only thus the streamwise Reynolds stress could be estimated from

$$\overline{u'^2} = \frac{1}{T}\int_0^T u'^2 \, \mathrm{d}t \neq 0 \tag{2.6}$$

Note that for incompressible flows it is common practice to simply refer to $\overline{u_i' u_j'}$ as the Reynolds stress tensor.

The fluctuating velocity signal, $u_i'(t)$, also provides insight into the turbulent energy content of a flow. The wide range in scales of turbulent eddies produce a corresponding range of velocity fluctuation frequencies in a fixed-point measurement: larger scale eddies produce lower frequency fluctuations while smaller scale eddies produce higher frequency velocity fluctuations. Hence, a Fourier transform, where f is the frequency, provides a frequency spectrum of the turbulent energy contained at each wavelength within the fluctuating velocity signal, thereby describing the turbulent energy distribution of the turbulence. Thus, the frequency spectrum, Φ, provides a simple means by which to observe changes and/or additions to turbulent energies where

$$\Phi = \left| \int_0^T u'(t) e^{-2\pi i f t} \mathrm{d}t \right|^2 \tag{2.7}$$

Note that, although the full turbulent kinetic energy turbulence spectrum contains contributions of all three components of velocity, here it is estimated using only the streamwise component of velocity as this was the only measured velocity component.

It follows that the contribution to the Reynolds stress from the velocity fluctuations can be recovered from the frequency spectrum through

$$\overline{u'^2} = \int_0^\infty \Phi \mathrm{d}f. \tag{2.8}$$

2.3 Turbulent Wall-Bounded Flow

The turbulence picture becomes complex for turbulent wall-bounded flow due to the confinement introduced by the surface. This confinement results in an additional scale separation problem being introduced, related to the distance from the surface, y. The result is a range of sublayers over which viscosity and inertial influences play competing roles.

Due to the various sources of influences throughout each of the turbulent sublayers, analytically (and even computationally) solving or computing flow velocities in turbulent wall-bounded flow is a difficult endeavor. However, with scaling arguments, one can identify important flow characteristics within defined regions of the turbulent flow by utilizing relatively few dimensionless parameters.

In classical scaling, the turbulent layer is composed of two principle regions that follow distinct scalings: a near-wall region following inner scaling, where viscous effects are of strong significance, and an outer region following outer scaling where viscous effects are negligible. Between these two regions there is believed to be a region of overlap, where both inner and outer scalings are valid. In the near wall region the characteristic velocity and length scales are taken to be u_τ and δ_ν, respectively (referred to as inner scaling), where $u_\tau = \sqrt{\tau_w/\rho}$ is the friction velocity. In the outer region the characteristic length scale is the turbulent layer thickness, δ, and the

characteristic velocity continues to be u_τ, since u_τ is related to the wall shear stress which affects the entire velocity field (referred to as outer scaling). Figure 2.2 shows an example using inner scaling to scale the profiles of streamwise mean velocity, $\overline{u}$, measured in a turbulent channel flow. Note, that it is common practice to use a + to indicate scaling using u_τ and δ_ν such that $y^+ = y/\delta_\nu$ and $\overline{u}/u_\tau = u^+$. The collapse of the velocity profiles demonstrates the success of scaling in understanding these types of flows and reveals key features of the velocity profiles of different Reynolds numbers within the near wall region. Further discussion of scaling methods can be found in Zagarola and Smits (1998)[7].

Classical scaling has led to the identification of sublayers within the turbulent wall layer, seen in figure 2.3. In fully turbulent, wall-bounded flow, the near-wall region is composed of three basic layers: the viscous sublayer ($0 \leq y^+ \leq 5$), where fluid viscosity dominates other effects; a buffer layer ($5 \leq y^+ \leq 30$), in which the viscous and turbulent shear stresses are both dynamically significant; a logarithmic layer ($y^+ = 30$ to $y/\delta \cong 0.15$), in which the effects of turbulent shear dominate. This is followed by an extensive outer wake region ($0.15 \leq y/\delta \leq 1$) that is strongly dependent on the boundary conditions and follows outer scaling. Note that the logarithmic layer can also be observed in outer scaling, the result of its formation from the overlap of both inner and outer scaled eddies. Hence the region $y^+ > 30$ to $y/\delta \cong 0.15$ is also referred to as the overlap layer.

The exact definition and ranges of these layers is still a matter of debate[8], however it is widely agreed that within the turbulent wall region there is a viscous sublayer followed by an overlap region where much of the turbulence is produced.[9][8]

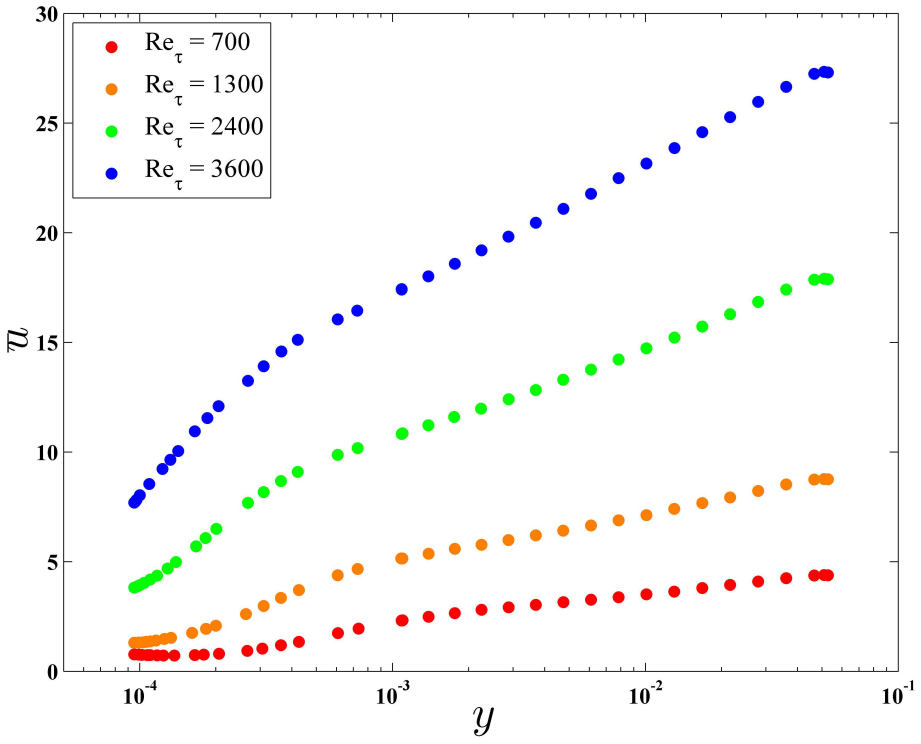

(a)

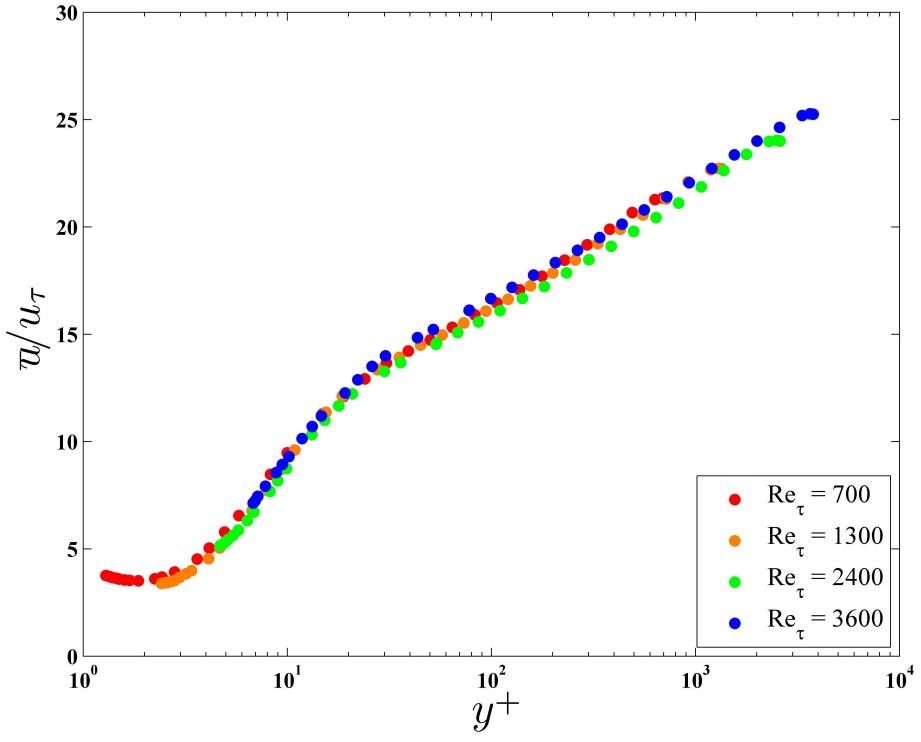

(b)

Figure 2.2: Mean velocity measurements shown in m/s and m (a) and using inner scaling (b).

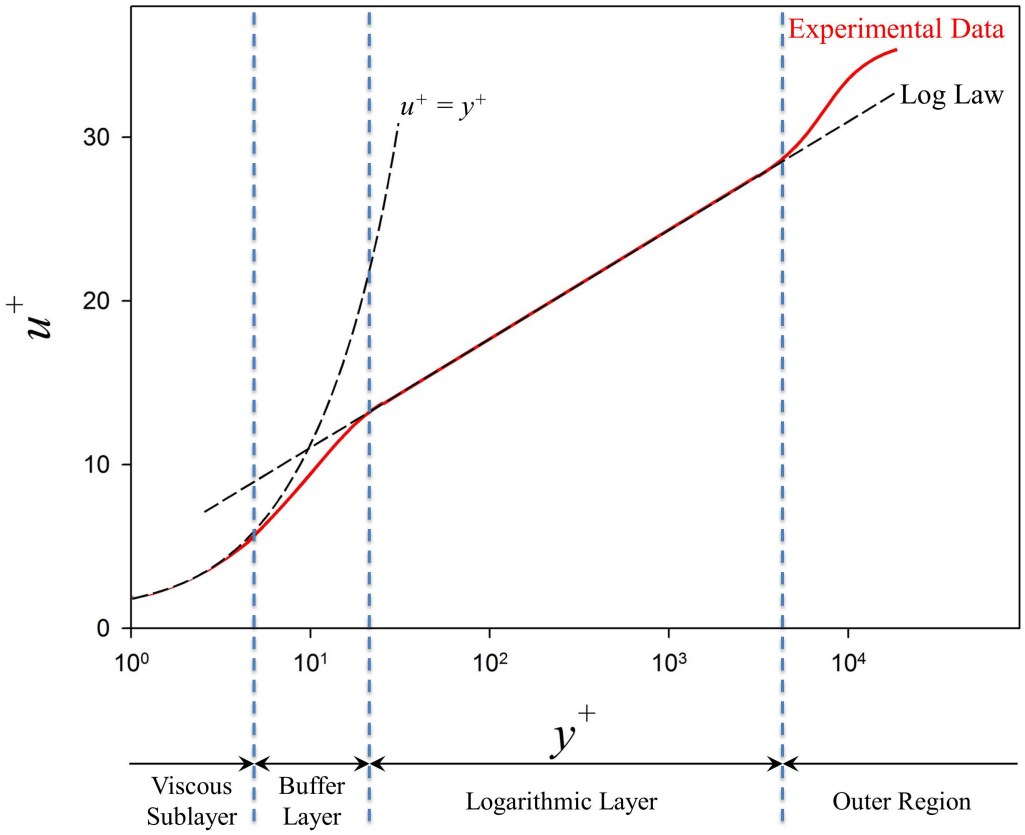

Figure 2.3: Sublayers within the turbulent wall layer.

CHAPTER 3 MOTIVATION AND RELATIVE RESEARCH

The application of nanowires has begun to show substantial promise in many fields including electric devices such as batteries[10][11], photovoltaics[12][13][14][15], and semiconductors[16][17]. The mechanical relevance of nanowires has also been indicated by recent studies in pressure sensing [18] and energy harvesting [19][20][21][22], though the capability of these wires in turbulent fluid flows has yet to be explored.

In recent studies, nanoscale surfaces exhibited beneficial properties in laminar flow, using carbon nanotube arrays (CNTs).[23][24] However these nanoscale surfaces are fragile and do not withstand the higher stresses of turbulent flow. Collaborating researchers at the University of Florida developed new synthesis methods to construct more durable Barium Titanate ($BaTiO_3$) nanowires that withstand the higher stresses accompanying higher velocity flows.

The research presented here is motivated by the potential for using thesee new piezoelectric nanowire coated surfaces to manipulate turbulent wall-bounded flow. However, due to their size, nanoscale materials are typically immersed within the viscous sublayer, where their influence on the flow is negligible. To influence bulk flow properties, any effects from surface structures must be transported out of the viscous sublayer into the buffer layer where much of the turbulence is produced. This is because small disturbances within the viscous sublayer, such as those created by surface roughness, are damped out by viscous effects within this region before reaching the buffer layer. Therefore, passive nanowires extending only into the viscous sublayer are predicted to have little influence on bulk turbulent properties. How-

ever, it may be possible that by dynamically actuating the nanowires, kinetic energy could be transported out of the viscous sublayer and into the buffer layer, thereby influencing turbulence production and modifying the turbulent flow field. The objective of this thesis is therefore to demonstrate the ability of dynamically actuated nanowires, actuated with nanoscale amplitudes, to transport momentum out of the viscous sublayer.

Within turbulent wall-bounded flow, higher surface shear stresses are caused by coherent vortical structures that draw high momentum fluid close to the surface, thus producing high shear stress. If these turbulent eddy motions can be modified and reduced the turbulent shear stresses and skin friction can be reduced. Turbulent property modification through the use of boundary surface manipulations has been demonstrated by numerous researchers, notably Jung *et al.* [25], Choi *et al.* [26, 27], and Bilgen *et al.* [28].

3.1 Oscillating Surfaces in Flows

Extensive study has been conducted suggesting the possibility of reducing skin-friction drag of the turbulent flow boundary layer by oscillating a wall in the spanwise direction. Jung *et al.* (1992)[25] were the first to suggest this using direct numerical simulation (DNS) on turbulent channel flow. They calculated that a maximum drag reduction of 40% could be obtained through transverse wall oscillation. Their inner-scaled velocity profile was shifted upward, implying the viscous sublayer was thickened as a result of the wall oscillation. They also observed a reduction in turbulence intensity of up to 35%.

Similar experimental studies were later conducted by Laadhari *et al.* (1994)[29]. They investigated the turbulent boundary layer and demonstrated the turbulence reduction resulting from the spanwise wall oscillations. They also observed that at an oscillation frequency of $f^+ = 0.01$, there were considerable decreases (up to 45%) in

velocity fluctuations for $y^+ < 200$. This experimentally confirmed the DNS research of Jung *et al.*.

In another DNS study at relatively low Reynolds number, Choi *et al.* (1994)[26] used selective suction and blowing to apply an oscillating velocity at the bounding wall surface. The oscillating wall velocity had an instantaneous y magnitude opposite to the y component of the flow velocity at a location $y^+ = 10$. They observed an increase in the scale of the eddy structures in the near wall region which led to a 25% drag reduction. An even greater reduction in turbulence was observed when they relaxed the no-slip boundary condition and imposed a spanwise velocity oscillation at the wall that was 180° out of phase with the spanwise z compenent of velocity at $y^+ = 10$, leading to a drag reduction of 30%. A combination of both wall-normal and spanwise velocity oscillation at the wall resulted in a relaminarization of the flow which may by attributed to the low Reynolds number of the simulation.

Additional experimental research performed by Choi and Graham (1998)[30] extended the possibility of flow control through wall oscillations by studying drag reduction in pipe flow using circular oscillations around the pipe's longitudinal axis. Conducted on fully turbulent pipe flow, researchers indicated that the turbulent drag in turbulent pipe flow can be reduced by up to 25% through circular oscillations. Similiar DNS studies of oscillations in pipe flow by Fatica (1997)[31] and Quadrio and Sibilla (2000)[32] showed the wall oscillations effectively modified the near-wall turbulent structures providing this reduction in wall shear stress.

Further study was carried out by numerous other researchers, notably Choi *et al.* (1998)[33], Dhanak and Si (1999)[34], Berger *et al.* (2000)[35], and Choi and Clayton (2001)[27], detailing the effects of oscillating surfaces on turbulent structures. Their research suggested the effects of oscillating surfaces are not only dependent upon the oscillation period but the amplitude of oscillation. Relatively large magnitude oscillations, $\Delta z^+ = 400$, were required to obtain significant turbulence modifications.

Implementing large scale spanwise oscillations into the bounding surface, although relatively easy to implement in simulations is challenging to do in practice. Thus there is a need to develop new actuators capable of imparting surface motion into the flow.

3.2 Actuated Surfaces in Flows

Developed in the early 1900's, piezoceramic actuators are capable of producing small amplitude, high frequency disturbances. Compared to other wall boundary manipulators, effects of piezoelectric actuators on wall-bounded flow have not been thoroughly studied. Jacobson and Reynolds (1995)[36] first investigated the use of piezoelectric actuators to control disturbances in a laminar boundary layer. Their actuator consisted of piezo-ceramic cantilevers mounted flush with the wall, placed over cavities to produce counter-rotating streamwise vortices in the wall region of the flow. Their apparatus induced substantial disturbances in previously imposed turbulent structures, which led to a reduction of wall shear by 8%. These results suggest that turbulent structures generated through mechanical actuation, though limited in scale, could affect turbulent structures over a wide range of scales, such as those observed in fully turbulent flow.

Subsequently, Blackwelder, Liu, and Jeon (1998)[37] implemented unimorph, piezoceramic actuators that were mounted on a pre-existing wall in a fully developed, turbulent flow. They employed a delta wing shape actuator operating at frequencies of $0.01 < f^+ < 4$ with amplitudes between $0 < \Delta y^+ < 16$. Under these conditions they found that the actuator produced a strong spanwise velocities that delayed the breakdown of streamwise vortices in the laminar boundary layer. Blackwelder and Jeon (2000)[38] later continued their study using the same the delta wing actuator, examining its influences on a turbulent boundary layer. A more detailed examination using hot-wire anemometry revealed that large scale, near-wall velocity disturbances from the actuator lead to a reduction in magnitude of the streamwise velocity fluctuations

downstream by up to 30%.

More recently, actuated surfaces have been shown to demonstrate the ability to initiate laminar to turbulent flow transition. Bilgen *et al.* (2011)[28] implemented a total of nine unimorph, piezocomposite benders distributed spanwise across the leading edge of a variable camber airfoil to investigate flow manipulation, exhibited in the lift and stall for low Reynolds number flows. They found that at an actuation frequency of 125 Hz, there was a substantial decrease in flow separation resulting in an increased lift of 18.4%. Kumar *et al.* (2011)[39] developed a nonlinear piezoelectric plate model to provide sufficient control to manipulate the flow conditions for transition from laminar to turbulent flow.

3.3 Nanoscale Materials in Flow

Nanoscale materials have only recently been studied for their possible effects on fluids and flow properties. Ming *et al.* (2011)[23] conducted experiments in laminar flow to verify the superhydrophic properties of surfaces coated with carbon nanotube forests. They observed a slippage effect between the liquid and nanotube surfaces which could yield a dramatic reductions in drag. Chen *et al.* (2011)[24] observed how carbon nanotubes might be used to influence low Reynolds number flows. In laminar flow they found that a reduction of viscosity around the carbon nanotubes due to local heating was significantly weakening the drag force.

To date, the investigation of nanowire arrays' influence on flow has been limited to low Reynolds number, laminar applications. However, it is in the manipulation and control of turbulent flow that these surfaces hold the greatest potential for practical application.

CHAPTER 4 EXPERIMENTAL FACILITIES, INSTRUMENTS, AND MEASUREMENT PROCEDURES

4.1 Experiment Overview

As described by the preceding chapter sections, there is great potential for reducing turbulent skin friction through manipulation of the bounding surface. Piezoelectric nanowire arrays arranged on the surface could potentially be used to produce this manipulation through, for example, traveling waves in the wires. However, due to their small size, these nanowire arrays would be immersed in the viscous sublayer, and the nanoscale amplitude of their actuation might not able to introduce forcing into the buffer layer, where the drag-producing motions exist.

To determine whether it is feasible for nanowire arrays to introduce forcing into the buffer layer, an experiment was conducted in which a nanowire array was located on the bounding surface of a turbulent channel flow wind tunnel. In this experiment, the nanowire array itself was not actuated. Instead, the array was adhered to a piezoelectric substrate which was used for actuation. Changes to the turbulence by the motion of the nanowire array was then measured to determine the magnitude and extent of the influence of the array.

4.2 Turbulent Flow Channel

The channel used for this research study was designed to create fully-developed turbulent, plane Poiseuille flow while maximizing Reynolds number within the constraints of laboratory space. Fully-developed turbulent Poiseuille flow is a form of

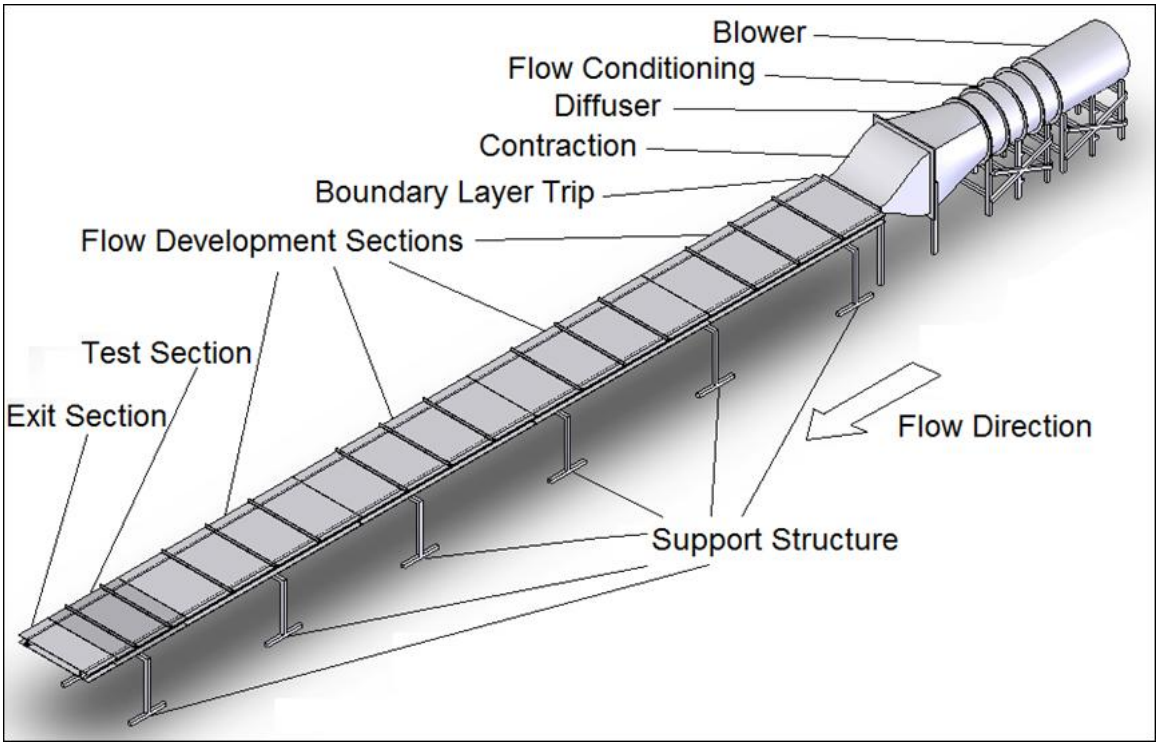

Figure 4.1: Turbulent channel flow facility used in this investigation.[1]

canonical wall-bounded flow where the turbulent flow develops between two parallel surfaces, resulting in a one-dimensional flow where the statistics depend only on the distance from the surface y.

The tunnel (illustrated in figure 4.1) had a total length of 17.9 m, leaving approximately 1 m of empty space at the channel exit to allow the flow to freely exit without stagnation or back pressure. The channel length was broken down into four major sections: the blower and flow conditioner, flow diffuser, contraction section, and working section.

4.2.1 Blower and Flow Conditioner

Air was forced through the channel using a Peerless Electric Model 245 Centrifan in-line blower. With an internal diameter of 0.84 m, the blower can displace 2.8 m^3/s when operating at 1445 RPM. A Reliance 5.6 kW 3- phase motor with controller was used to power the fan.

After exiting the fan, the air passed through a 1 m long, 0.84 internal diameter settling section. Within this section were six fine-mesh screens that reduced flow disturbances introduced by the blower blades. The resulting flow was therefore approximately steady and uniform when exiting this section.

4.2.2 Flow Diffuser

In order to pass the air from the circular cross-section blower and flow conditioner into the rectangular cross-section working section, a flow diffuser changed the 0.84 m diameter cross-section inlet to a 0.91 m^2 cross-section over a length of 0.91 m. This resulted in a maximum sidewall angle of 13 ° relative to the mean flow direction, ensuring the flow did not separate inside this section.

4.2.3 Contraction Section

While exiting the flow diffuser in a rectangular cross-section, the flow needed to be contracted down to the size of the test section. The goal of this section was not only to accelerate the flow and achieve the desired cross-section, but to produce low turbulence, steady flow at the exit. In order to simplify this section, the width of the flow diffuser was matched to the width of the working section, making only two-dimensional contraction necessary. If not properly designed the contraction could have resulted in unsteadiness and separation in the flow.

Following Monty (2005)[40], the contraction employed a cubic curve near the entrance followed by a parabolic curve near the exit. Given a well conditioned source at the inlet, this design ensured no separation of the flow and a uniform, low turbulence flow at the exit. The dimensions of the contraction section were 1.05 m in length with the cubic and parabolic curves meeting 0.76 m from the entrance. This geometry yielded a contraction area ratio of 9:1, which was within the suggested range described by Tavoularis (2005)[41] and Barlow, Rae and Pope (1999)[42] for

disturbance rejection.

The contraction was constructed out of 1.6 mm thick aluminum sheet. At the exit of the contraction section, 44 mm aluminum angles were spot welded to serve as flanges to connect the subsequent working section and then sanded down to remove defects on the interior surface. Automotive body filler was then added to correct for any possible indentations that could disturb the flow from one section to the next.

4.2.4 Working Section

Following the contraction section was the working section. In order to achieve a fully turbulent Poiseuille flow, the channel must be of adequate length to eliminate streamwise velocity gradients. The span must also be sufficiently larger than the height to eliminate spanwise velocity gradients at the channel centerline. Monty (2005)[40] concluded that velocity spectra are no longer streamwise dependent after a length of $128H$, where H is the channel height. Furthermore, Dean (1978) demonstrated that a width to height aspect ratio of 7:1 is the minimum to produce a two dimensional flow at the channel centerline. At a total length of 13.9 m, a channel height of $H \approx$0.1 m achieved the $128H$ length requirement. A channel width of 0.15 m was then implemented to exceed the width to height ratio requirements at 9:1.

The channel's working section was therefore 13.9 m long, 0.1016 m high, and 0.9144 m wide. It was constructed from 6.35 mm thick 3003 aluminum plates to form the upper and lower surfaces and 101.6 mm high outward-facing 6061 aluminum C-channels for sides. The working section contained five distinct components: support structures, boundary layer trip section, flow development section, test section and exit section.

4.2.4.1 Channel Support Structures

To support the channel and avoid unwanted deflections along its length four 7.62 m long, 0.15 m wide aluminum I-beams were placed underneath the channel in two pairs spanning its length. Rather than parallel, two pairs of I-beam were placed in V's along the length of the channel whose ends were positioned approximately 0.41 m apart at their upstream end and approximately 0.72 m apart at their downstream end.

To support these I-beams, six 1.2 m wide, 0.81 m tall support frames were manufactured from 5 cm square steel tubing. Each support frame was equipped with four leveling feet to allow small adjustments to the height of the working section along its length.

4.2.4.2 Boundary Layer Trip Section

After exiting the contraction section, the flow entered a 0.3 m long area that creates a regular laminar-turbulent transition point. This was achieved through the use of a 50 mm long streamwise section of 120 grit adhesive backed sandpaper followed immediately by a 100 mm long streamwise section of 60 grit adhesive backed sandpaper around the entirety of the inside surface of the channel. Located 76 mm downstream from the contraction exit, this trip design introduced perturbations to the flow over a range of 0.11 to 150 mm, greatly increasing the probability of initiating turbulent transition along the bounding wall layers.

4.2.4.3 Flow Development Section

After introducing turbulence, the fluid passed through a 12.192 m flow development section ensuring fully developed turbulence before reaching the test section. This length was manufactured in four separate 3.048 m long sections constructed from 6.35 mm thick 3003 aluminum plate and 101.6 mm high 6061 outward facing

aluminum C-channels. To join these sections, 1.2 m long sections of 6061 aluminum C-channel were bolted in place along the channel, outside the sidewall C channel, in the direction of the flow. These additional C-channels not only maintained a positive connection between the sections but also provided additional rigidity to the channel. Each section was sealed together using silicone sealant to eliminate pressure leaks and ensure constant mass flux through the entirety of the channel.

In order to deter deflections in the upper surface of the channel during operation, three 50 mm x 50 mm 6061 aluminum angle pieces were attached to the top of each of the four sections. Affixed spanwise, perpendicular to the flow direction, these pieces provided additional stiffness to the upper surface. Additional angle pieces were placed at the section joints to ensure smooth transition between each section. This was unnecessary on the lower surface as the supporting I-beams provided ample stiffening.

4.2.4.4 Test Section

Following the flow development section was the one meter long test section where measurements were conducted. Using the same 6.35 mm thick 3003 aluminum plate for upper and lower surfaces the test section was built similar to the rest of the working section. However, to enable optical measurement techniques, the sidewalls were constructed from 12.7 mm thick clear polycarbonate sheets, keeping the same inner, cross sectional dimensions as the rest of the working section. This feature was also used to visually verify measurement locations and equipment functionality. Two 50 mm x 50 mm 6061 aluminum angles were used to prevent upper surface deflection as before.

A 0.15 m diameter hole was located in the center of the lower surface to allow an equal diameter insert containing measurement apparatus to be placed in the channel with minimal disturbance to the flow.

4.2.4.5 Exit Section

In order to ensure exit conditions did not interfere with flow conditions and pressure gradients within the test section, an additional 0.51 m exit section was added downstream of the test section.

4.3 Instrumentation

A diagram showing the instrumentation and connectivity is provided in figure 4.2. For this study a single sensor hot-wire probe was used to measure wall-normal profiles of velocity. A Pitot static tube and temperature sensor were used in conjunction with the hot-wire probe to calibrate the probe and correct it for temperature changes. These instruments were attached to the removable channel insert to more easily insert them into the flow with consistent results.

4.3.1 Pitot-Static Tube

For hot-wire calibration purposes a Dwyer model 167-6 Pitot-static tube was used over the course of this study. This model of Pitot-static tube was 3.2 mm in diameter, had a 152 mm insertion length and a 38.1 mm long streamwise-aligned element. The total pressure hole was placed at the vertical center of the channel, 50.8 mm above the lower surface, 20 mm off the centerline. The Pitot tube was connected to a pressure transducer via 1.5 mm internal diameter PVC tubing.

4.3.2 Pressure Taps

Two 1.3 mm diameter pressure taps were drilled into the removable insert for use in conjunction with the Pitot tube and pressure transducer for static pressure measurements during hot-wire sensor calibrations. Located 15 mm on each side of the channel spanwise centerline, these taps were drilled from the interior surface to

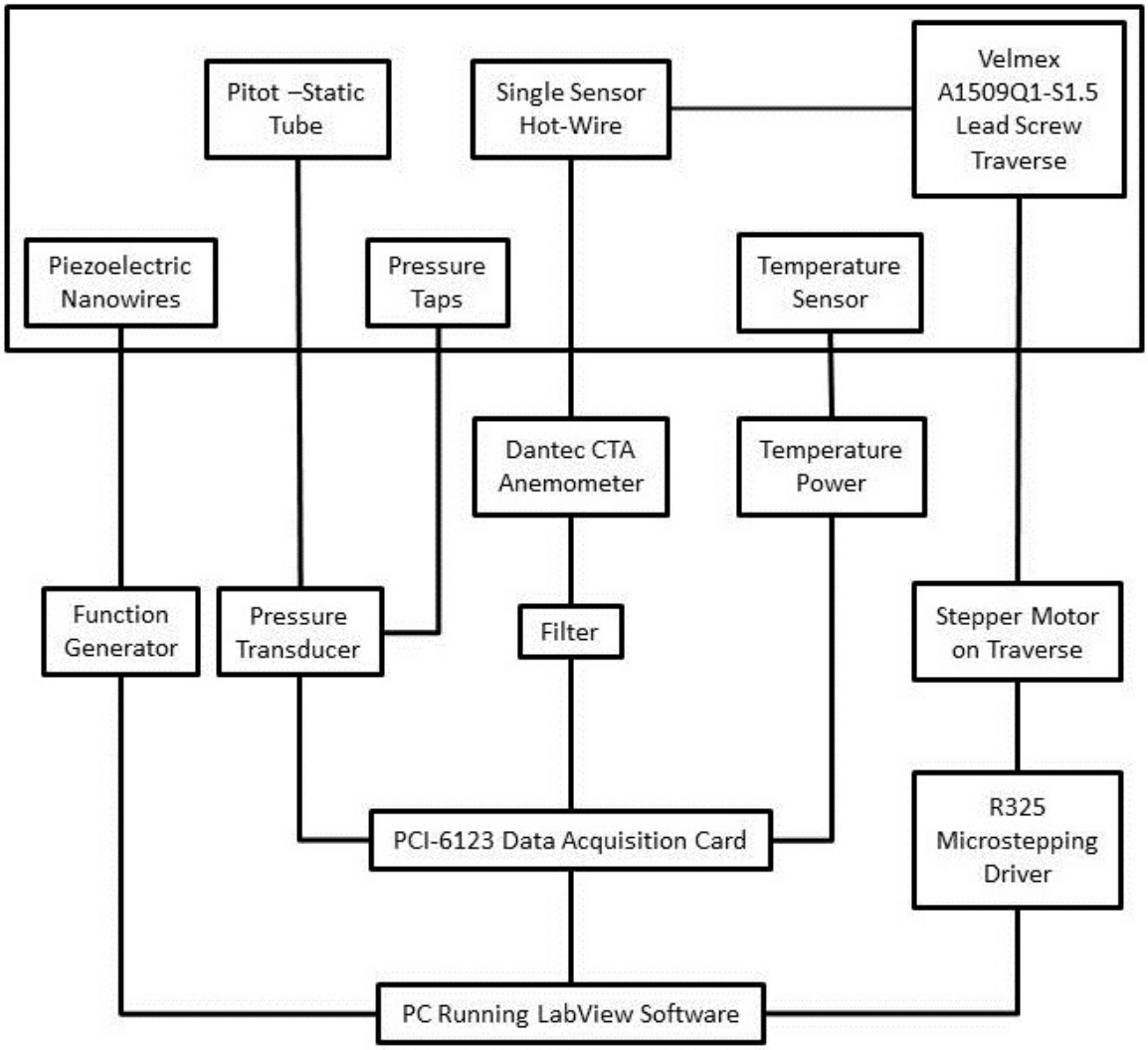

Figure 4.2: Diagram of instrumentation and connections used during hot-wire measurements.

minimize burrs and defects on the surface that could cause flow disturbances. Outside the channel, the two pressure taps were combined into one using a simple plastic T-junction fitting. The combined pressure taps were then connected to the pressure transducer using 1.5 mm diameter internal diameter PVC tubing.

4.3.3 Pressure Transducer

Pressure data from the Pitot-static tube and pressure taps was acquired using an NIST calibrated Omega PX653-03D5V high accuracy low pressure, differential, laboratory transducer with a range of 0-748 Pa. In order to simplify the zeroing of the transducer, a two-way valve was placed in the tubing from the Pitot tube to allow the high and low pressure inputs of the transducer to be quickly connected via a separate line.

4.3.4 Temperature Probe

Air temperature was monitored inside the channel using an Omega THX-400-AP thermistor air probe. Equipped with a radiant energy shield, this probe had a perforated tip to expose the thermistor bead to air flow for fast, accurate measurements. The temperature probe was powered by an Omega DP25-TH-A precision thermistor controller with digital display and linearized analog output. This temperature measurement system had a combined accuracy of ± 0.2°C.

The temperature probe was also located on the removable insert containing the rest of the measurement instruments. A 4.8 mm hole was drilled into the insert allowing only the sensor tip to be introduced into the flow 0.61 m downstream from the inlet of the test section, and 0.05 m from the spanwise channel centerline.

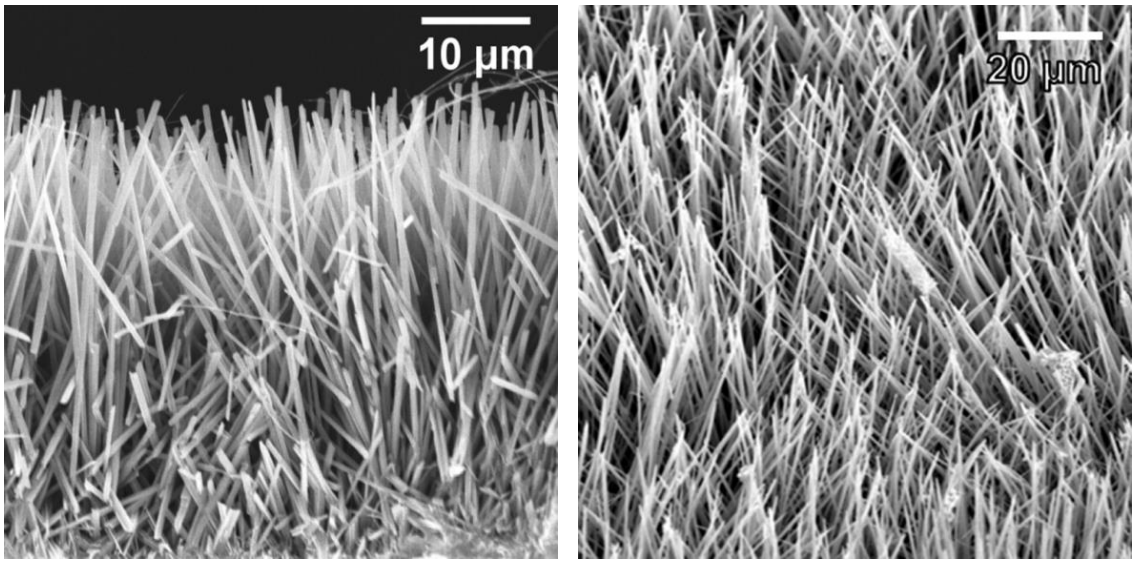

Figure 4.3: Scanning electron microscope image of the $BaTiO_3$ nanowires.[2]

4.3.5 Piezoelectric Nanowire Arrays

The piezoelectric nanowire arrays were synthesized and obtained from collaborators at the University of Florida. A hydrothermal process was employed to grow these extra long, vertically aligned arrays of Barium Titanate ($BaTiO_3$) nanowires. The dimensions of the nanowires were determined by scanning electron microscopy (SEM) to have individual wire lengths, l_w, of approximately 45 μm and individual wire diameters of approximately 600 nm, seen in figure 4.3.

To allow actuation of the arrays, the nanowires were adhered to a circular Lead Zirconate Titanate (PZT-5H) piezoelectric wafer. Two wafer sizes were used over the course of this study: 6.4 mm and 12.7 mm diameter. These wafers were then placed into a plastic inserts, with height adjustment via a simple threaded screw, that allowed for the PZT disk to be placed flush with the bounding wall of the turbulent flow channel with only the nanowires protruding into the flow. The plastic inserts were themselves inserted into a 12.7 mm hole drilled into the center of the removable instrumentation insert.

4.3.6 Function Generator

To excite the PZT disk, a sinusoidal electric field was applied using a BK Precision 20 MHz Sweep Function Generator model 4040a. The function generator output signal was passed through an amplifier in order to actuate the PZT wafer at an a frequency of 10 kHz and an amplitude of 70 V-rms. The actuation signal could be externally triggered using a TTL signal from the attached PC running LabView software.

This periodic excitation signal expanded and contracted the PZT disc and attached nanowires in all directions. These isotropic motions produced nanowire oscillations at the actuation frequency, $f_{act} = 10$ kHz, with amplitudes ranging from zero to a maximum of, 40 μm, the length of the nanowires. This actuation frequency was chosen to maximize the amplitude of the nanowire motions as determined for the properties of the PZT piezoelectric wafers to which the nanowires were attached.

4.3.7 Hot-Wire Probe

To allow near-wall measurements, a single-sensor, miniature, boundary-layer hot-wire probe was used. These probes were manufactured by soldering platinum-rhodium (90% Pt - 10% Rh) Wollaston wire to the probe prongs then etching a small portion of the wire with a nitric acid solution exposing a small portion of the platinum-rhodium wire. The etching was achieved by affixing the probe to a micro-positioner then lowering the wire into a small bubble of 15% nitric acid solution that formed at the tip of a syringe as it flowed out vertically. This exposed a $l = 0.5$ mm long, $d = 2.5$ μm diameter sensing section of wire resulting in an l/d ratio of aproximately 200. As set forth by Ligrani and Bradshaw (1987)[43], an l/d ratio greater 200 will minimize end conduction effects on the hot-wire frequency response characteristics. The hot-wire probe was positioned on the measurement apparatus insert such that the hot-wire was 4.35 mm downstream from the center of the nanowire insert. Because the relative

location of the hot wire to the center of the nanowire array was constant throughout this study, the streamwise measurement locations were 1.15 mm downstream from the trailing edge of the 6.4 mm diameter nanowire array and directly over the 12.7 mm diameter nanowire array.

4.3.8 Hot-Wire Anemometer

A Dantec Streamline Research constant temperature anemometer (CTA) system was used to drive the hot-wire probe. This system had the option of a 1:20 internal bride ratio or a 1:1 bridge ratio that required an external resistor to set the overheat ratio and balance the system. The 1:1 bridge ratio was used in this study to better control the overheat ratio with an external variable resistor manufactured by Bourns, Inc. The Dantec CTA also had the ability to condition output signals by inputing user defined gains and DC-offsets to the input signals, as well as high and low-pass filtering. The system was controlled via custom-written LabView software through serial communication to an attached PC.

4.3.9 Filter

Instead of the on-board filter of the Dantec CTA, an external filter was used to filter the output from the CTA to allow freedom in choice of filtering frequency. A Krohn-Hite Model 3905a eight pole, multichannel filter was used to analog filter the anemometer output at 30 kHz.

4.3.10 Probe Positioning

To accurately control the movement of the hot-wire probe, a custom precision traverse system was used, composed of a lead screw traverse, microstepping driver, and optical encoder. A Velmex A1509Q1-S1.5 lead screw traverse with a 1 mm per rotation pitch was utilized and powered by a Lin Engineering 417/15/03 high

accuracy stepper motor through a belt with a 1:2 increase in pulley diameter for higher movement resolution. This motion was controlled with a Lin Engineering R325 microstepping driver which, when combined with the other traverse components, yielded a potential position resolution of 5 nm per step. An Acu-Rite SENC50 E 5/M DD9 0.5 A156 linear encoder tracked the motion with a 0.5 μm resolution and accuracy down to ± 3 μm. The encoder output, a quadrature signal, was then passed through a USDigital LS7184 quadrature clock converter chip, then combined into a single clock pulse signal with a companion TTL direction signal.

To achieve a hot-wire position, within 100 μm relative to the wall, without contact (which would destroy the hot-wire probe), an electrical contact limit switch was designed into the positioning system by mounting a bar on the moving portion of the lead screw drive that would contact a micrometer mounted on the stationary portion of the lead screw drive. When the two were in contact, a 5 V signal was output, alerting the software of the probes set position. After positioning the hot-wire probe, the micrometer was then be set to that position creating an initial measuring distance while, at the same time, preventing the hot-wire from traversing below this wall normal distance. Therefore, by manipulating the micrometer, the initial probe position was maintained constant for each set of measurements.

A Titan Tool Supply Z-axis ZDM-1 measuring microscope was used to measure the initial wall-normal position of the hot-wire above the surface with an accuracy of ± 5 μm. The importance of near wall measurements is detailed by Orlu *et al.* (2010). For this study in particular, the near wall measurements are of the utmost importance, for the effects of the nanowires are most likely to be seen in the viscous sublayer contiguous to the bounding wall. A diagram of the measurement apparatuses and relative location on the removable insert is provided in Figure 4.4.

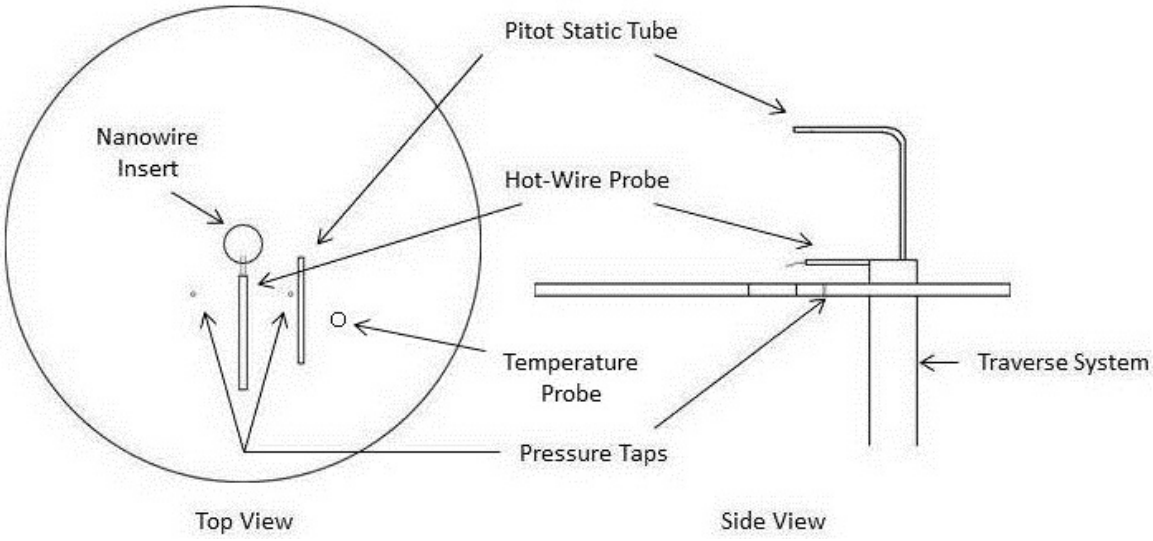

Figure 4.4: Diagram of insert containing measuring apparatus. Figure not to scale.

4.3.11 Data Acquisition

Analog signals from the pressure transducer, Dantec CTA, and temperature sensor were digitized using a National Instruments PCI-6123 data acquisition card mounted in a desktop PC. This acquisition card sampled up to 8 analog channels at 500 kHz and 16-bit resolution simultaneously across each channel with zero time-shift between channels. In addition, this acquisition card had analog and digital triggering, 8 hardware-timed digital I/O lines, and two 24-bit counters that were used for experimental control. Inputs and outputs to and from the acquisition card first passed through a National Instruments BNC-2110 connector block.

4.3.12 Experiment Control

The computer in which the data acquisition card was installed, acted as the control center for the whole experiment. To reduce human error and increase repeatability of the measurements, the experimental control and data acquisition process was completely automated and managed through the use of custom written LabView script. The script read in desired probe locations from a user input file and moved the hot-

wire probe to the desired wall-normal location by outputting a square-wave signal to the stepper motor controller, all the while monitoring the limit switch to ensure the hot-wire probe does not accidentally contact the surface. The software simultaneously counted pulse and direction signals output from the clock converter chip to monitor feedback data from the linear encoder, tracking the probe's location. Once the probe was at the proper wall-normal position, the program turned on the function generator by outputting a 5 V TTL gating signal to the external trigger on the function generator, actuating the nanowire array, and initiating sampling the analog hot-wire data at the desired rate and sample length. After the data acquisition is complete, the code recorded the voltages to a binary data file. Before moving to the next location, the LabView script stopped the function generator and took another set of hot-wire data to give an unactuated comparison at the same location. After the unactuated data acquisition, the software recorded the results in a binary data file and then moved the probe to the next measurement position.

4.4 Preliminary Measurements and Method Improvements

Many initial measurements were performed in order to improve procedures and achieve consistent, accurate results. Comparative data sets were taken in search of any possible sources of measurement deviation including: differences between the channels of the CTA, external bridge resistors, lengths of data acquisition time, and the hot-wires themselves. Certain procedures were also changed to eliminate possible sources of error. Originally, a full set of measurements was taken with the nanowires actuated before resetting the probe to the set position and taking a full set of unactuated data. Despite the precision of the probe traverse and positioning system, small errors in the probe position led to significant differences in the measured velocities as seen in figure 4.5.

To eliminate this error in probe position, both actuated and unactuated cases

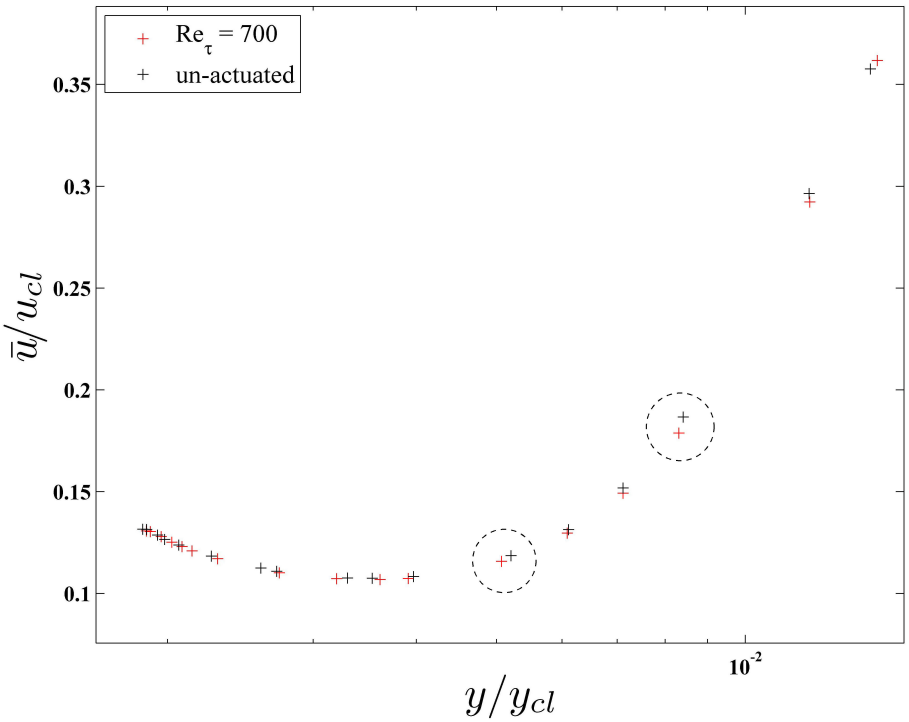

Figure 4.5: Position error in initial measurements.

were measured at each position before traversing the probe to the next measurement position, i.e. measurements were taken with the nanowires actuated then measurements are taken with the nanowires stationary before moving the probe to the next designated position.

Primary interest of this study focused on the nanowire effects in the near wall region, therefore a high concentration of velocity measurements are taken in this region. Initial measurements did not measure the outer region and instead only acquired data at the channel centerline. This is evident in some of the graphs of mean velocity and Reynolds Stress for the 6.4 mm nanowire array (figures 5.1(a) and 5.2(a)). Though not significant in the results or conclusions (all analysis of frequency and kinetic energy is performed on data taken within the near wall region), this procedure was later changed to take data across a full range of positions spanning the entire channel half-height

Measurements of velocity were originally digitized at a rate of 60 kHz. This coarse

rendering of the analog velocity signal caused higher levels of noise in the frequency spectra, Φ, surrounding the actuation frequency of 10 kHz. To remedy this the resolution of the velocity signal was adjusted until a final sample rate of 200 kHz was deemed sufficient for all data acquisitions. This increase further detailed the velocity signal and reduced the noise levels to better distinguish the effects of the nanowire actuations.

Through the investigation and elimination of conceivable sources of inconsistency a final procedure was achieved producing accurate and repeatable results.

4.5 Measurement Procedures and Conditions

Over the course of this research, streamwise velocity wall-normal profiles were measured using hot-wire anemometry. The single sensor hot-wire probe was aligned parallel to the wall, and velocity profiles were measured at the following Reynolds numbers: $\mathrm{Re}_\tau = \delta u_\tau/\nu = 700$, 1300, 2500, and 3600. These were obtained by controlling the centerline velocity of the tunnel, u_{cl}. This increase in Reynolds number from 700 to 3600 increased the kinetic energy of the flow while decreasing the viscous sublayer thickness, $\delta_s = 5\delta_\nu$, from 370 μm to 70 μm. The hot-wire probe was located along the spanwise center of the channel 0.61 m from the inlet of the test section and $126H$ downstream from the turbulence trip. A diagram of the hot-wire positioning can be seen in figure 4.6.

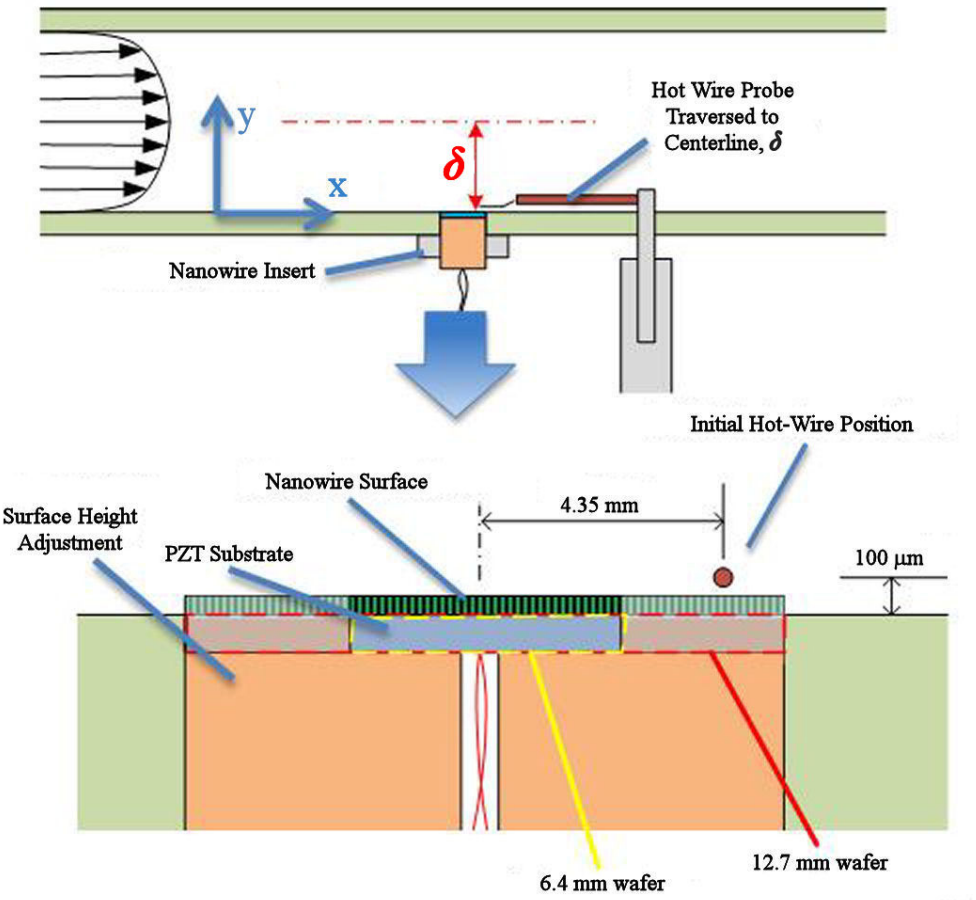

Figure 4.6: Diagram of hot-wire probe location relative to nanowire arrays. Figure not to scale.

Prior to each data acquisition, the probe was calibrated at the wall normal channel centerline,, y_{cl}, using the Pitot tube and temperature sensor (Sections 4.3.1 and 4.3.4). For each Reynolds number, a different number of calibration points, ranging from 7 to 23, was used in order to span the range of flow velocities. During calibration, the channel flow was given 15 seconds to stabilize after every velocity change, and before data collection initiated.

The resistance of the prongs and leads of the hot-wire probe was measured to be approximately 1.0 Ω. With this known, the Dantec anemometer was set to use a 1:1 bridge with an external resistor for bridge balancing in order to maintain an overheat ratio, $a = (R_w - R_0)/R_0 = 0.7$, where R_w is the sensor resistance at operating

temperature and R_0 is the sensor resistance at ambient temperature. This resulted in a measured square-wave response greater than 70 kHz. The output signals were then filtered at 30 kHz using the external filter (Section 4.3.9) and digitized at 200kHz using the data acquisition system (section 4.3.11). Output signal gain and offset voltages were set to maximize resolution of the analog signal preceding each set of measurements.

Calibration bridge voltage measurements were then corrected for any temperature fluctuations using Jorgenson 2002[44]

$$E_{corr} = \left(\frac{T_w - T_0}{T_w - T_a}\right)^{0.5} E_a \tag{4.1}$$

where E_a is the acquired voltage, T_w is the sensor hot temperature, T_0 is the reference temperature, T_a is the ambient temperature during acquisition, and E_{corr} is temperature-corrected voltage. Using this temperature-corrected hot-wire voltage and Pitot-static tube velocity measurements, a fourth order polynomial was used to fit a calibration curve. An example calibration curve is provided in figure 4.7.

The sensing length of the hot-wire probe, $l = 0.5$ mm, lead to a viscous scale wire length, $l^+ = 6.8$, 12.8, 24.7 and 35.8, at $\mathrm{Re}_\tau = 700$, 1300, 2500, and 3600, respectively. An initial wall-normal distance, y_0, of approximately 100 μm was set before each data acquisition utilizing the depth measuring microscope (Section 4.3.12). Data was taken at 36 wall-normal positions between y_0 and the channel centerline $y_{cl} =$ 52.6 mm $+y_0$, with a higher concentration of data points near the wall for greater resolution in this region. Flow velocity data was acquired at each position for 120 seconds with the nanowire arrays actuated followed by data collection for 120 seconds without actuation before moving to the next wall-normal position. A full listing of experimental conditions is presented in tables 4.1 and 4.2.

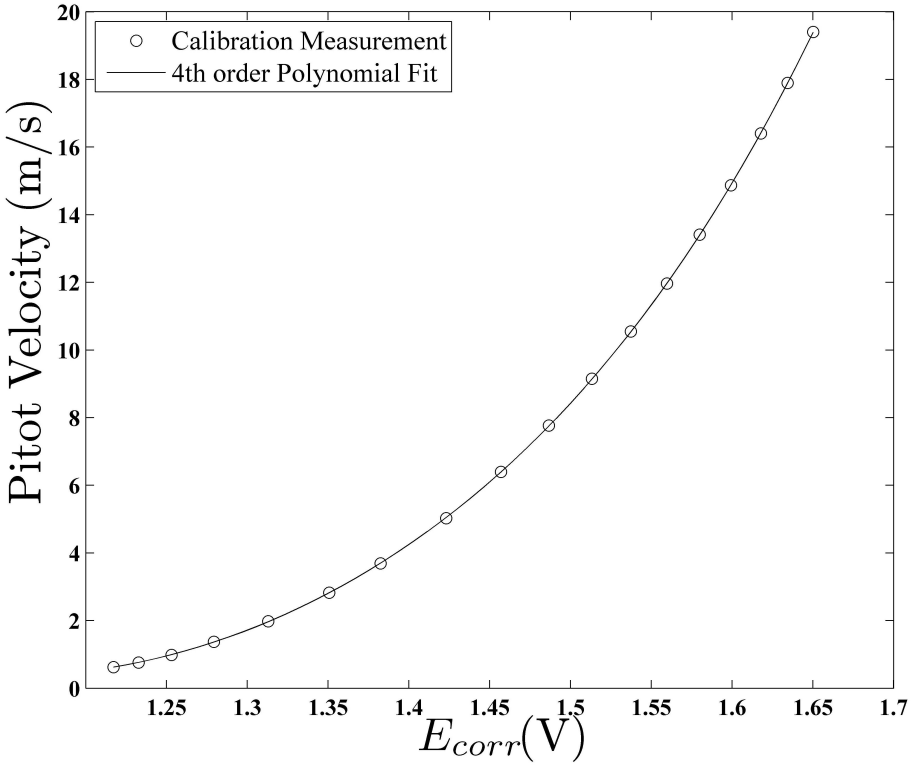

Figure 4.7: Example calibration curve from Re_τ = 2400.

Table 4.1: Experimental conditions for the 6.4 mm diameter surface.

Re_τ	Motor Frequency (Hz)	u_{cl} (m/s)	u_τ	δ_s (μm)	y_0 (μm)	Calibration Points	Anemometer Gain	Anemometer Offset (V)
700	11.7	4.7	0.2168	350	96	8	16	1.55
1300	21.3	8.9	0.3869	295	96	12	16	1.55
2400	40.4	17.4	0.7186	105	96	18	16	1.55
3600	59.6	27.6	1.1010	70	96	24	16	1.55

Table 4.2: Experimental conditions for the 12.7 mm diameter surface.

Re_τ	Motor Frequency (Hz)	u_{cl} (m/s)	u_τ	δ_s (μm)	y_0 (μm)	Calibration Points	Anemometer Gain	Anemometer Offset (V)
700	11.7	4.5	0.2056	370	96	8	32	1.22
1300	21.3	8.8	0.3859	195	96	12	32	1.27
2500	40.4	18.1	0.7454	100	97	18	16	1.55
3600	59.6	27.1	1.0830	70	97	24	16	1.55

CHAPTER 5 RESULTS AND DISCUSSION

5.1 Mean Velocity and Reynolds Stress Profiles

The hot-wire anemometer acquired streamwise velocity measurements as a function of time $u(t) = \overline{u} + u'(t)$. Figure 5.1 presents mean velocity profiles, $\overline{u}$, as a function of wall-normal distance. This provides a simple comparison of velocity for the actuated and unactuated cases of both the 6.4 mm and 12.7 mm nanowire surfaces. The mean velocity graphs display typical behavior expected from wall-bounded, turbulent flow. In the viscous sublayer, flow velocities exhibit a linear dependence on wall-normal distance, y, in accordance with the law of wall. This is followed by the overlap layer, which varies logarithmically with y. Note the logarithmic scaling of the abscissa, used to better detail the near wall region. For both the 6.4 mm and 12.7 mm cases, the mean velocity profile is unchanged when piezoelectric actuation is induced. This implies that the nanowires have no effect on the skin friction and hence, the macroscopic flow properties. This result is not surprising when considering the size and motions of the PZT wafer. The PZT discs expand and contract in all directions when actuated. These isotropic motions were not expected to affect the large scale flow properties or structures for the small amplitude motions of the nanowires.

The mean Reynolds stress profiles, $\overline{u'^2}$, for the 6.4 mm and 12.7 mm nanowire arrays are shown in figure 5.2. These plots show an obvious and expected peak where Reynolds shear stress and turbulence production is at a maximum within the buffer layer. However, they too exhibit little difference between the actuated and unactuated cases, further indicating no effect on the macroscopic flow properties.

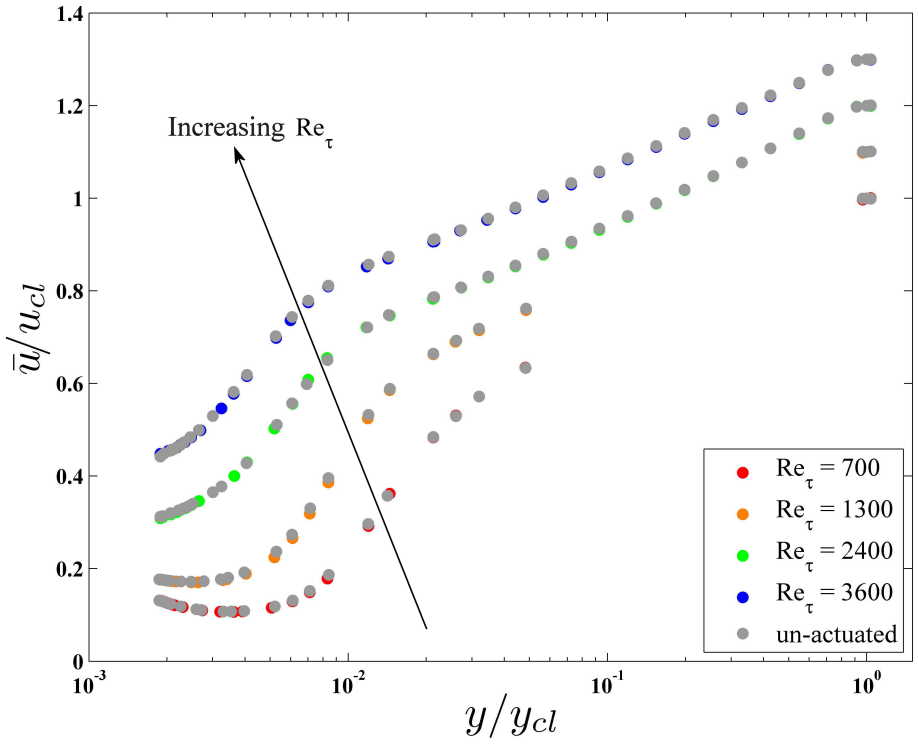

(a) *6.4 mm diameter surface*

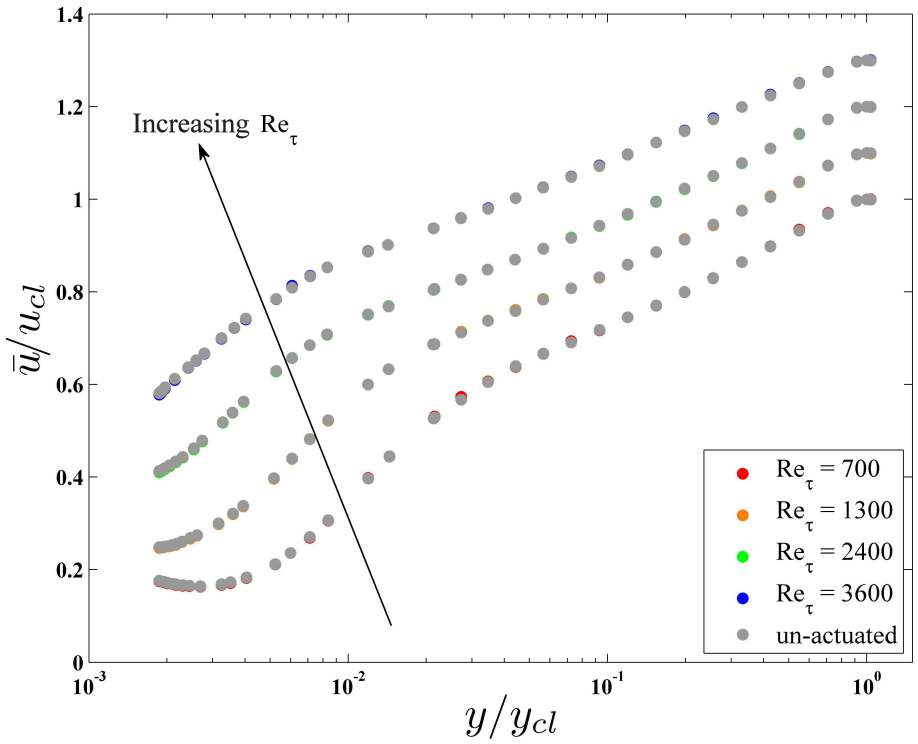

(b) *12.7 mm diameter surface*

Figure 5.1: Mean streamwise velocity profiles of both actuated and unactuated cases. Note: Successive profiles are shifted vertically .1 $\bar{u}/u_{cl}$ for clarity

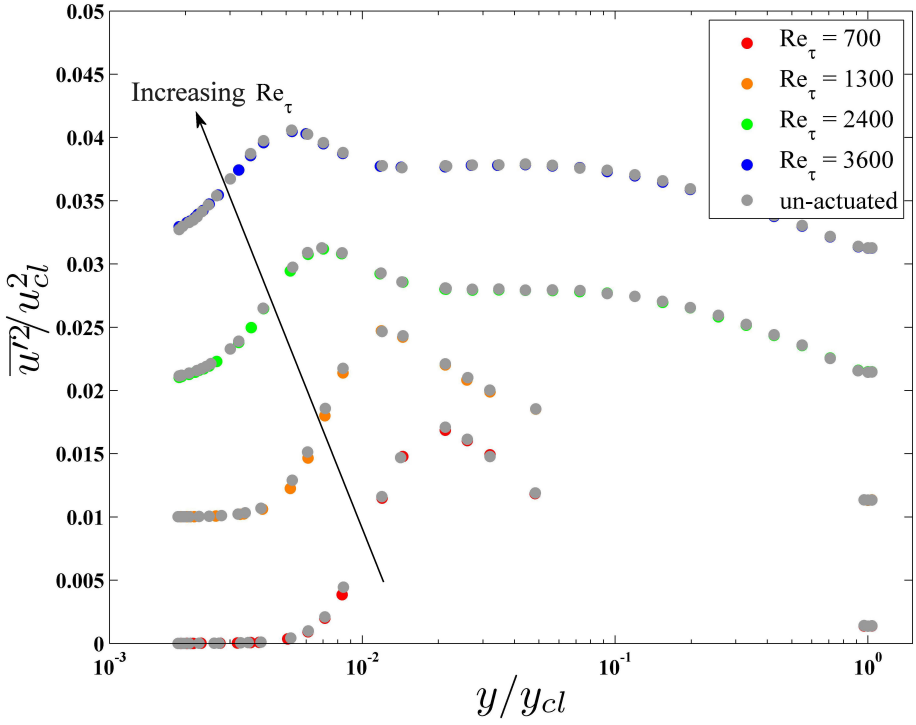

(a) *6.4 mm diameter surface*

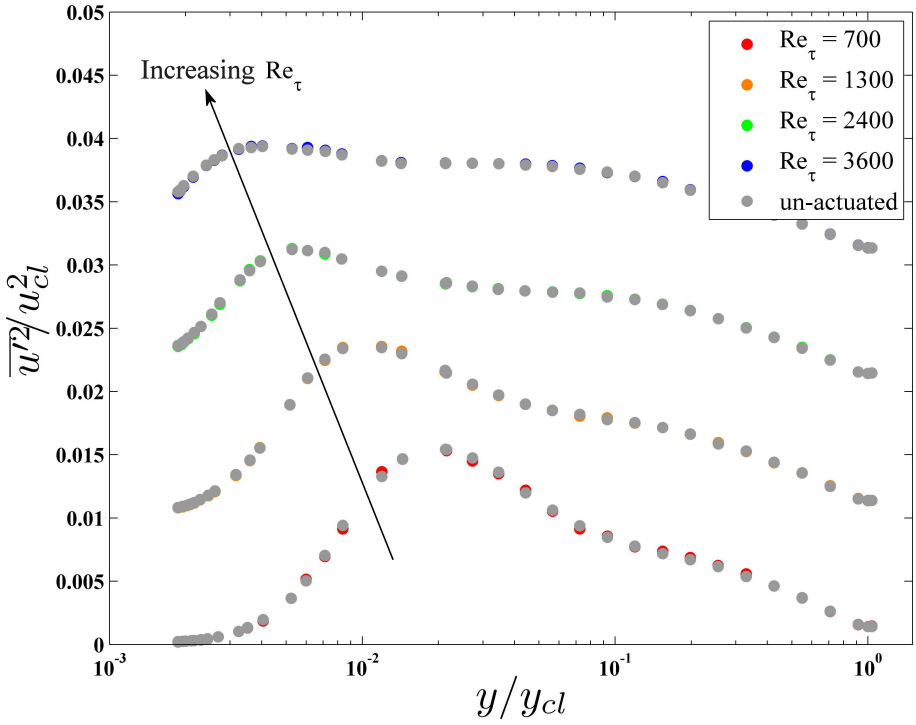

(b) *12.7 mm diameter surface*

Figure 5.2: Mean Reynolds stress profiles for both actuated and unactuated cases. Note: Successive Reynolds numbers are shifted vertically .01 u'/u_τ^2 for clarity

5.2 Frequency Spectra

The frequency spectra, Φ, presented in figure 5.3, display traditional features expected from turbulent, wall-bounded flow: an energy containing range of low frequencies corresponding to the large $O(\delta)$ turbulent eddies, a lower energy range at higher frequencies corresponding to the smallest $O(\delta_\nu)$ turbulent eddies, and a intermediary range of decreasing energies between the two corresponding to inertial cascade of the medial scale eddies. However, there is an obvious spike in the kinetic energy for the actuated case at the actuation frequency, f_{act}=10 kHz. This peak is evident within the buffer at the wall normal position $y^+ = 15$, the location of maximum Reynolds stress and turbulent production for smooth wall-bounded turbulent flow. Furthermore, this peak is present in frequency spectra of wall normal distances beyond the buffer layer at $y^+ = 35$ and is seen throughout the entire turbulent layer.

Also evident in these spectra is the increase of turbulence at higher frequencies following the increase in Re_τ. At the lowest Reynolds number, f_{act} lies outside of the range of energy containing turbulent frequencies, however at the highest Reynolds number, f_{act} is within this energy containing, turbulent frequency range. Energy added from the actuated nanowires is evident across all values of Re_τ. For the 6.4 mm nanowire surface, figures 5.3(a) and 5.3(c), as Re_τ and turbulent energy content increase, the influence of the nanowire surface, represented by the peak at the actuation frequency, decreases relative to the surrounding turbulent energies until at the highest Re_τ the peak is nearly indistinguishable from the surrounding turbulence. By comparison, the 12.7 mm nanowire surface frequency spectra, figures 5.3(b) and 5.3(d), display a much stronger peak is evident through all values of Re_τ showing greater influence of the actuated nanowire surface as a result of the larger actuated surface area.

Additionally, a second peak is evident in the spectra of the 12.7 mm surface at

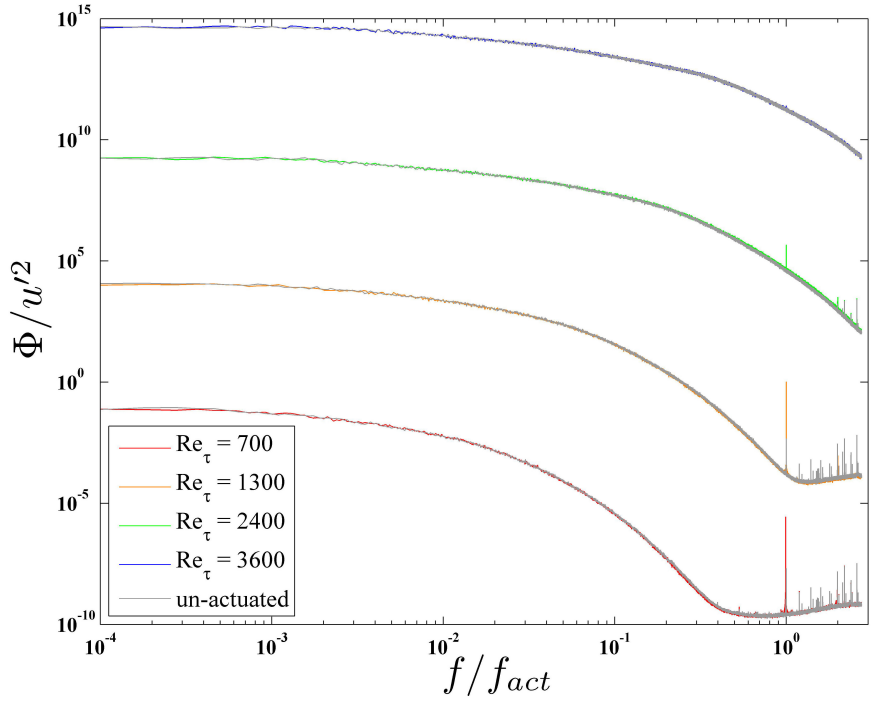

(a) *6.4 mm diameter at* $y^+ = 15$

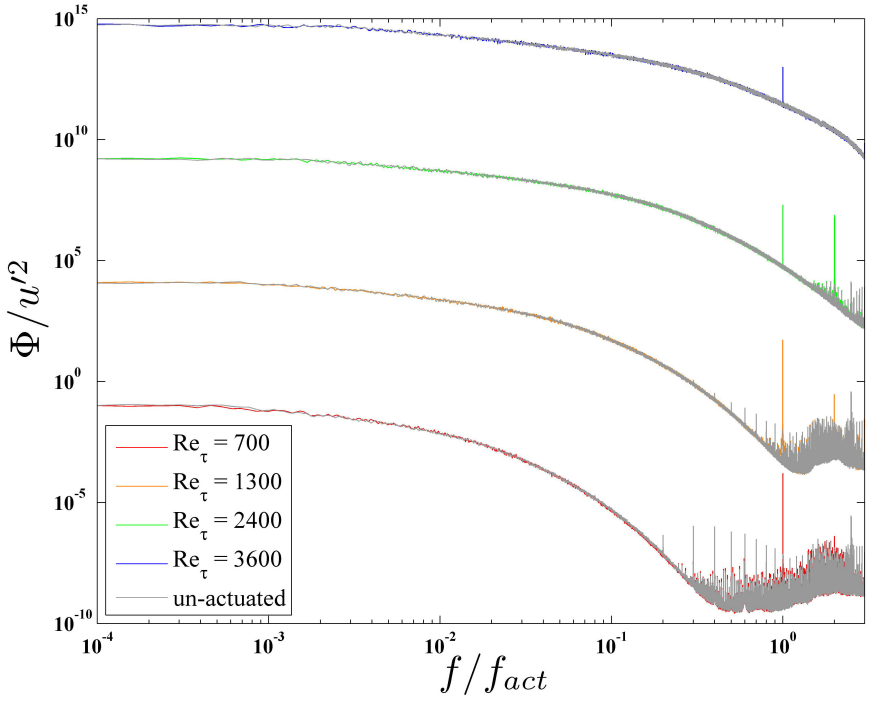

(b) *12.7 mm diameter at* $y^+ = 15$

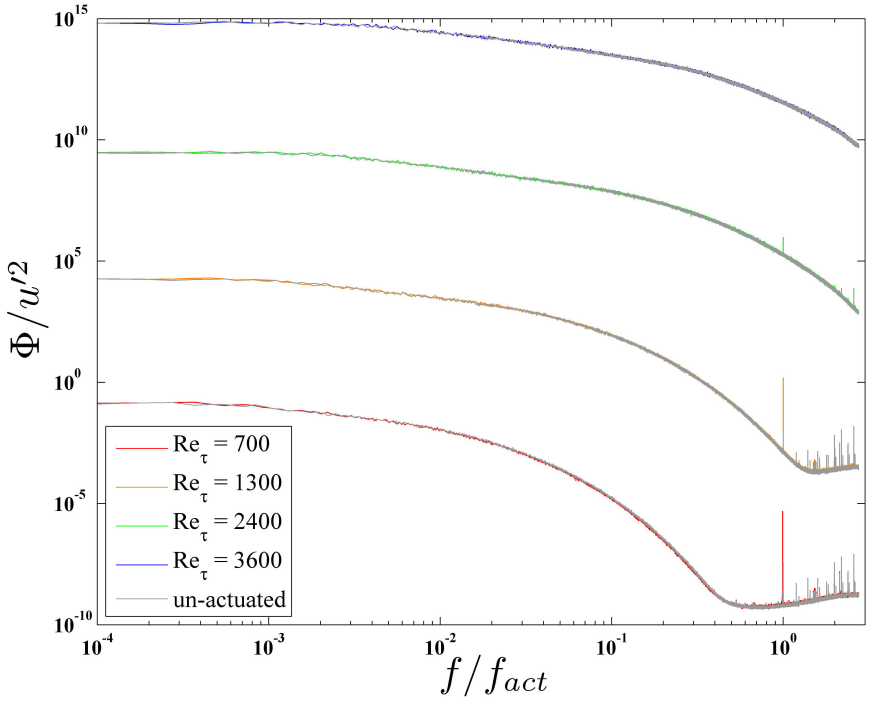

(c) *6.4 mm diameter at* $y^+ = 35$

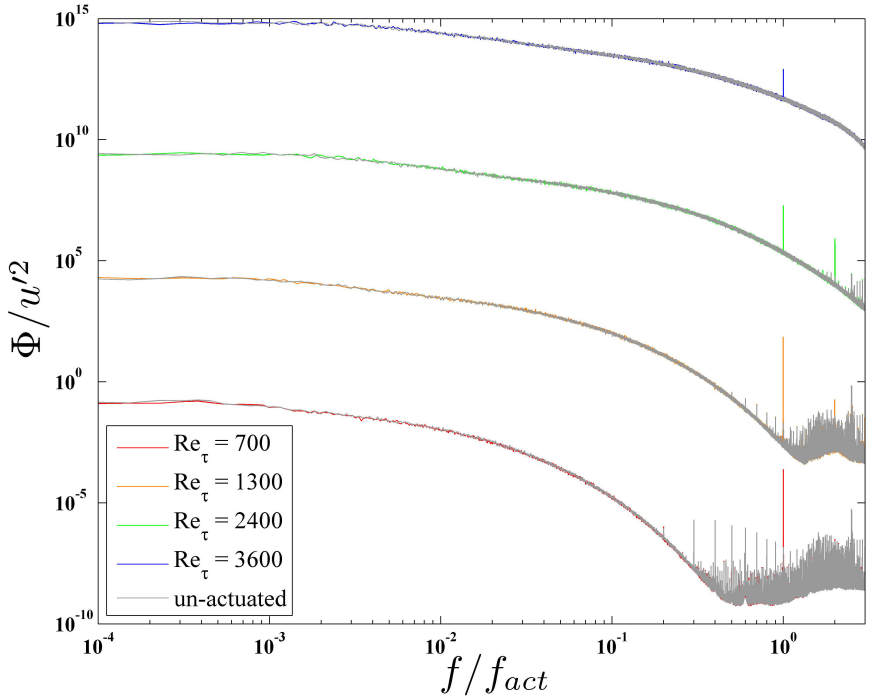

(d) *12.7 mm diameter at* $y^+ = 35$

Figure 5.3: Frequency spectra of actuated and unactuated cases:(a) and (b) at $y^+ = 15$*, (c) and (d) at* $y^+ = 35$*. Note: Successive spectra are shifted up six orders of magnitude for clarity*

$2f_{act}$, twice the actuation frequency seen in figure 5.4. This peak is believed to be the result of the transverse, spanwise motions induced by the PZT wafer and the lack of directional sensitivity of the single sensor hot-wire probe. The sinusoidal actuation creates both a positive and negative spanwise, z, component of velocity that is detected by the hot-wire probe as only an increase in velocity, u, twice per actuation period, producing a velocity increase and energy spike at twice the actuation frequency, $2f_{act}$. Thus, this second peak is interpreted as evidence of shear driven motions resulting from the nanowire actuations.

To better visualize the significance of the major peak at f_{act}, figures 5.5(a) and 5.5(b) show pre-multiplied versions of figures 5.3(a) and 5.3(b) respectively. This pre-multiplication of the spectra by the frequency compensates for the logarithmic scaling of the abscissa, providing a more useful visualization of the relative energy addition of each frequency to the total kinetic energy.

It is evident in figure 5.5(b) that, relative to the turbulent content, the magnitude of each peak and analogous kinetic energy contribution resulting from the nanowire surface actuation, clearly exceeds the kinetic energy contribution from any other frequency. However the net contribution, as reflected in the Reynolds stress profiles of figure 5.2, is relatively small.

The presence of these peaks at the specific wall-normal position, y^+=15, outside the viscous sublayer, shows that the influence of the actuated nanowires extended beyond the sublayer into the buffer layer and was detectable in the region of maximum turbulence production. This energy transport occurred without regard to the scale of the turbulence and also occurred whether the wires were deeply or shallowly immersed in the viscous sublayer. These observations are derived from the Reynolds number dependence of δ_ν such that the viscous sublayer thickness decreased from 370 μm to 70 μm as the Reynolds number is increased, while the nanowwire length, $l_w = 40$ μm, remains the same. This lead to an increase in the depth the nanowires extended into

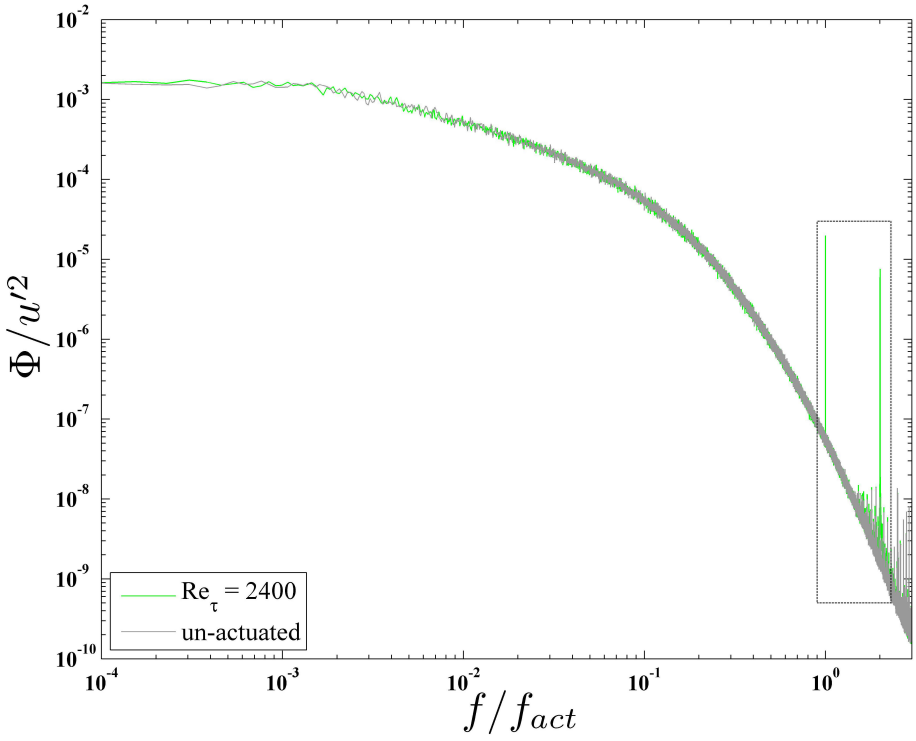

(a)

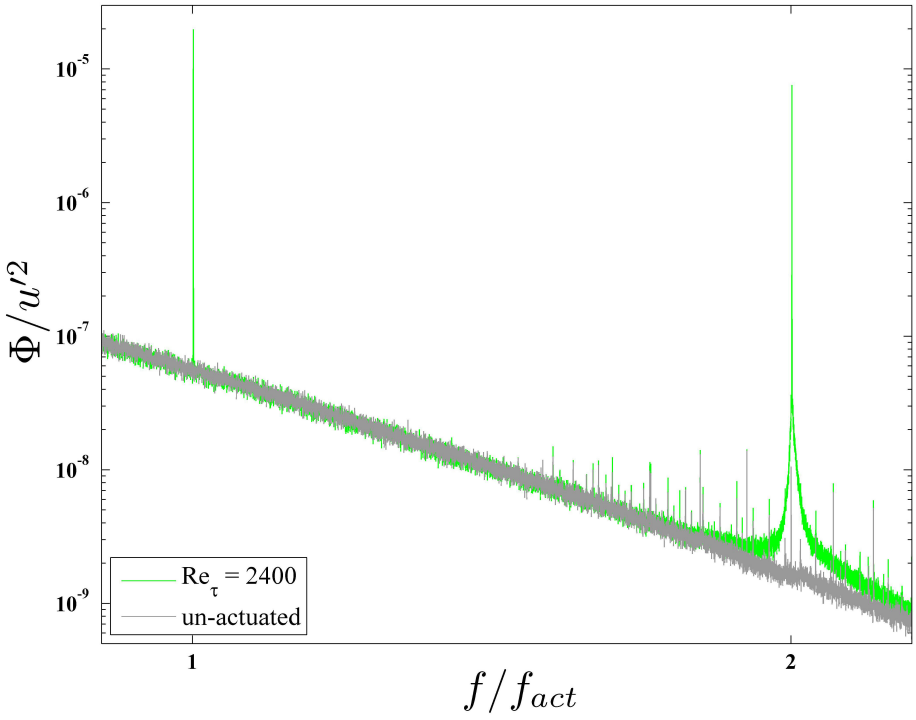

(b)

Figure 5.4: The spectral analysis for the 12.7 mm surface at Re_τ=2400, (a), with a detailed view of the region indicated by the dashed box, (b).

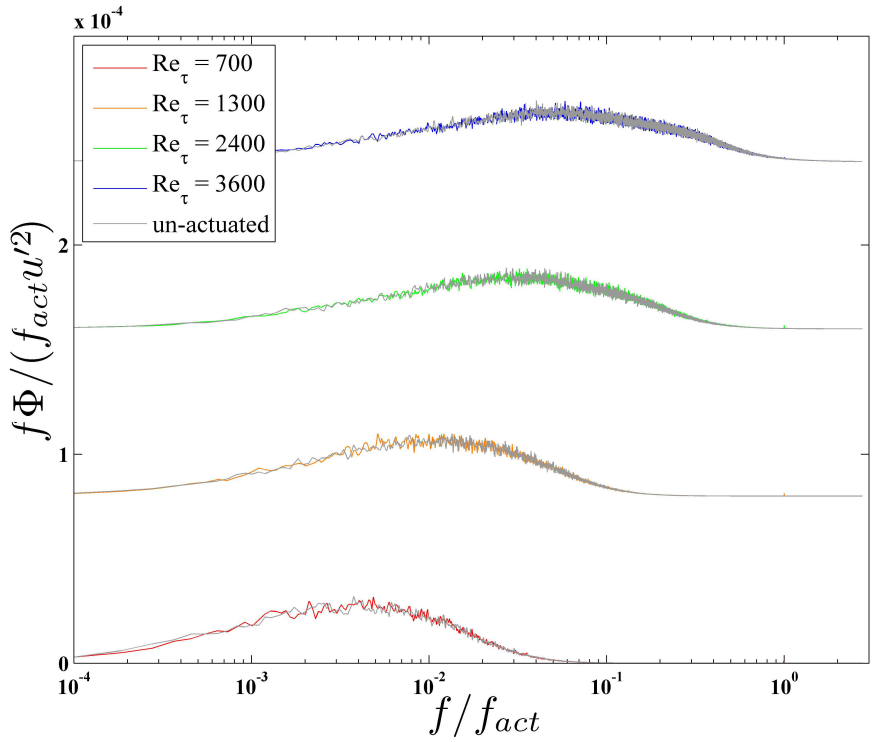

(a) 6.4 mm diameter surface

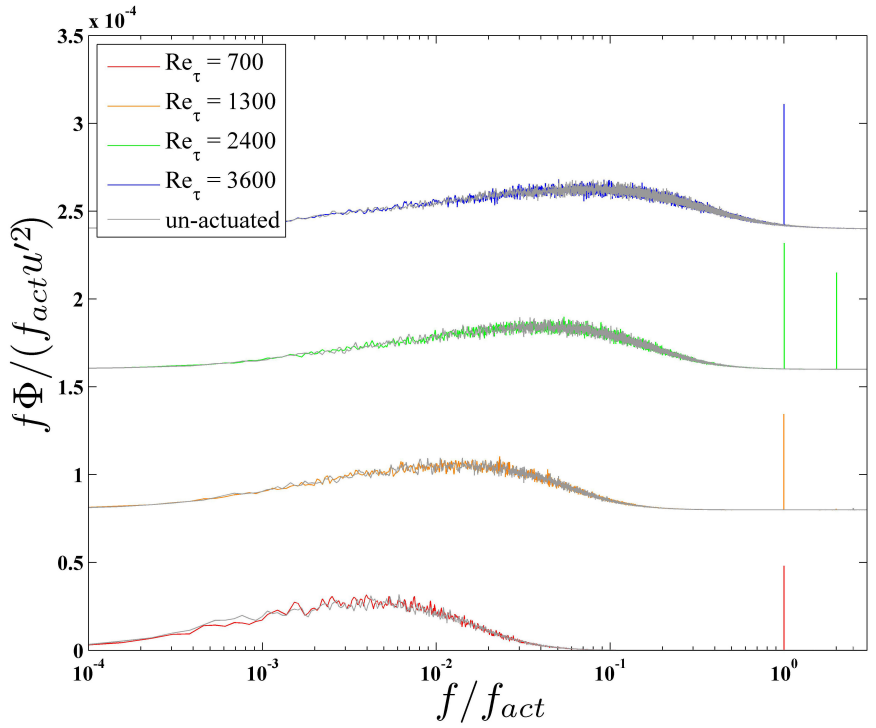

(b) 12.7 mm diameter surface

Figure 5.5: Pre-multiplied frequency spectra of actuated (a) and unactuated (b) cases at $y^+ = 15$. Note: Successive spectra are shifted up .8x10 $^{-4}$ for clarity

the viscous sublayer and can be quantified by the ratio of nanowire length to viscous sublayer thickness, r_w, which increased from .11 to .57 as Reynolds number increased from 700 to 3600.

To ensure that these peaks were the result of the nanowire movements and not electromagnetic interference from the function generator or amplifier, a data set was taken using a de-poled PZT wafer that had the electro-mechanical coupling removed such that no motion of the wafer would occur during actuation. In this experiment, no difference was observed in the spectra between the actuated and unactuated cases, indicating no additional electromagnetic interference entered the system during actuation and any variations between actuated and unactuated cases can be attributed solely to the nanowire surface movements.

5.3 Kinetic Energy Addition

To quantify the kinetic energy addition made to the turbulence from the actuated nanowire surface, integrals of the frequency spectra are taken across a range of frequencies $f_{act} \pm .01 f_{act}$ for both actuated, Φ_{act}, and unactuated, Φ_{un}, cases. The difference between these two integrals, $\Delta\Phi$, provides the additional kinetic energy injected to the flow by the actuated nanowire surfaces at the actuation frequency shown in figures 5.6(a) and 5.6(b) for the 6.4 mm and 12.7 mm nanowire surfaces, respectively.

$$\Delta\Phi = \int_{.99 f_{act}}^{1.01 f_{act}} \Phi_{act} \mathrm{d}f - \int_{.99 f_{act}}^{1.01 f_{act}} \Phi_{un} \mathrm{d}f \tag{5.1}$$

The kinetic energy addition shown in figure 5.1 reveals that the energy contribution from the actuated nanowire surfaces increased with Reynolds number. Furthermore, the kinetic energy contribution has a non-monotonic relation with wall-normal distance, y, near the wall. This indicates a lack of direct correlation between kinetic

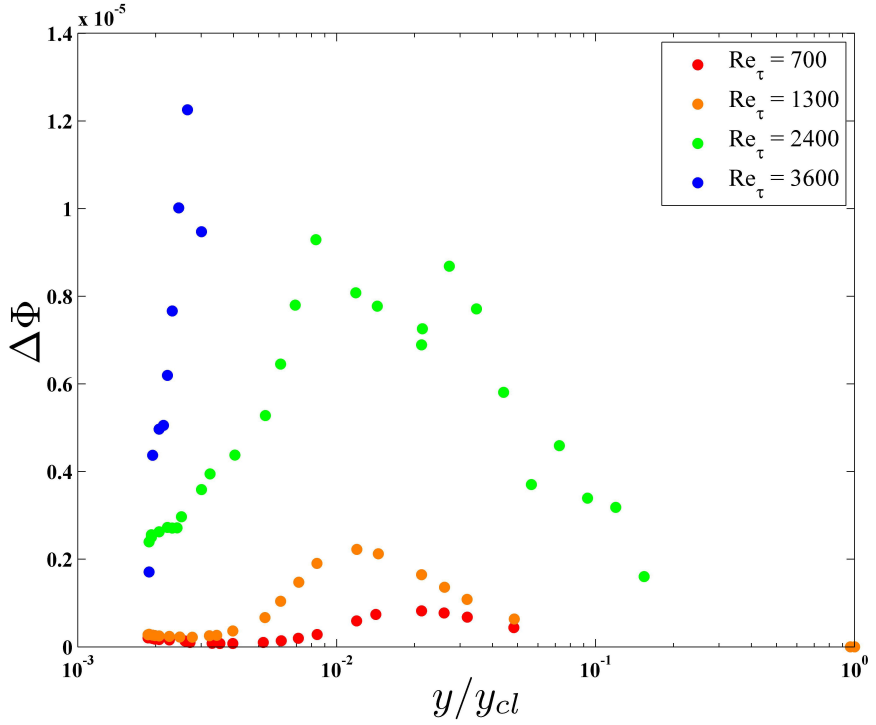

(a) *6.4 mm diameter surface*

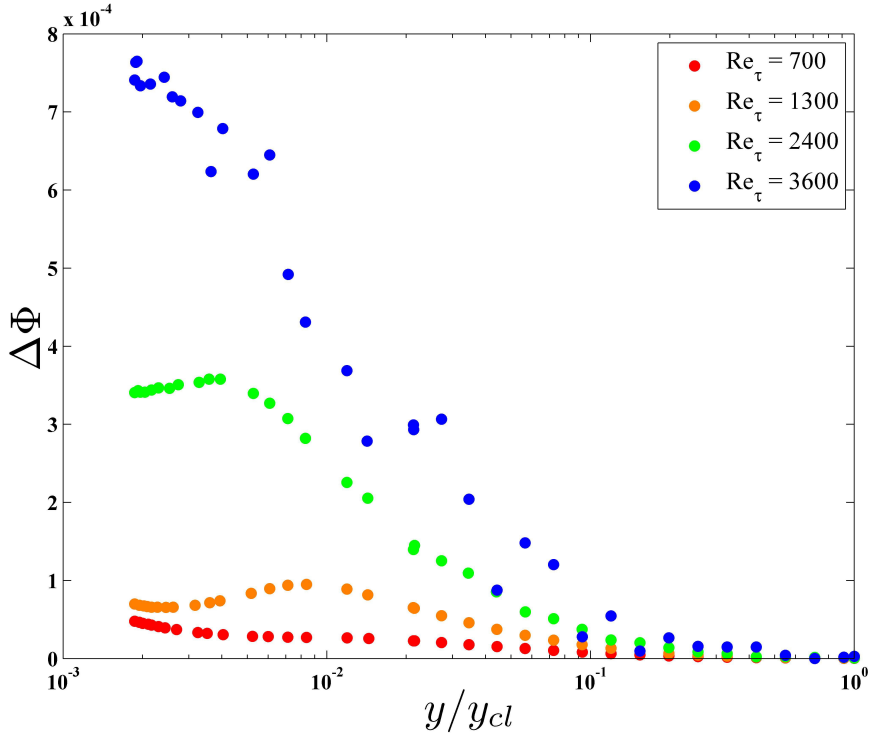

(b) *12.7 mm diameter surface*

Figure 5.6: Kinetic energy added to the turbulence due to nanowire surface actuation.

energy addition and wall-normal distance within this region. Further away from the wall, kinetic energy addition decays steadily with increasing wall-normal distance. In the absence of turbulence, kinetic energy addition from an oscillating surface decays monotonically throughout the wall layer as distance from the actuating surface increases (as shown by Stoke's second problem).[45] Since there was no change to the energy input into the nanowire array across the course of this study, this non-monotonic behavior and increase in added kinetic energy with Re_τ indicates that the nanowire induced motions are not merely added linearly to the flow but the efficacy of the nanowires to impart kinetic energy addition is dependent upon the flow conditions. This not only implies that the nanowire motions were not overwhelmed by the magnitude of the turbulence resulting from increases in Reynolds numbers, but also the nanowire motions were interacting with turbulence itself.

When the actuating surface size was increased from 6.4 mm to 12.7 mm (an increase in surface area by a factor of four) the kinetic energy addition increases by almost two orders of magnitude. It should be noted however that the hot-wire measurement location is not changed with each surface. While the measurements with the 12.7 mm nanowire surface are taken directly above the actuating surface, measurement are taken slightly downstream from the trailing edge of the 6.4 mm diameter nanowire surface. (see Section 4.6)

When the results of figures 5.6(a) and 5.6(b) are re-normalized using inner scaling, shown in figures 5.7(a) and 5.7(b), the dependence of kinetic energy addition on Reynolds number can be seen.

From these plots, it is evident that there is an approximate collapse and decay of the added kinetic energy profiles for wall-normal distances $y^+>15$. This decay initiates from a peak located at $y^+=15$, the point of maximum streamwise Reynolds stress and turbulence production for smooth walled turbulent flow. The friction velocity, u_τ, used to scale these graphs was measured in previous studies on this tunnel utilizing

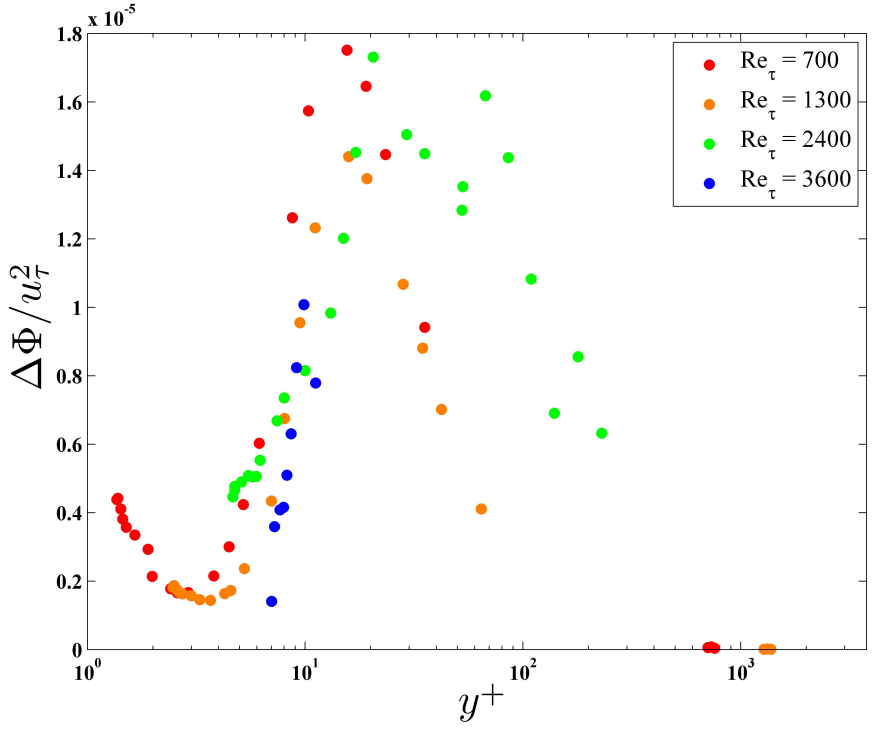

(a) 6.4 mm diameter surface

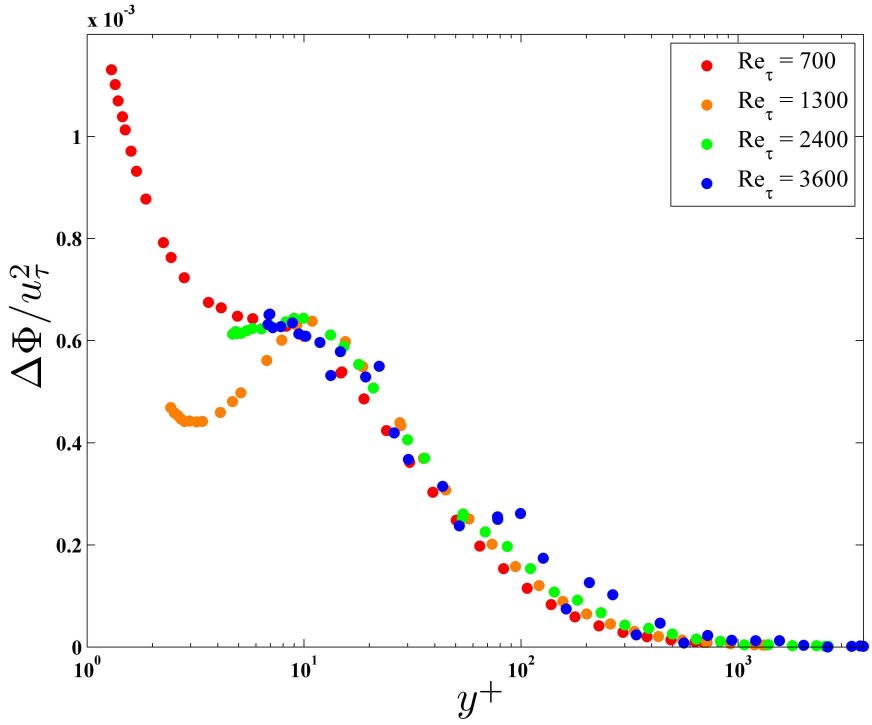

(b) 12.7 mm diameter surface

Figure 5.7: Additional kinetic energy injected into the turbulence due to nanowire surface actuation normalized using inner scaling.

pressure taps upstream of the test location. The scaling with u_τ does not reflect any wall shear stress alteration resulting from the actuated nanowire surface and can therefore be considered only using turbulence properties of the tunnel for scaling (independent of nanowire actuation). The measured kinetic energy addition, resultant from nanowire surface actuations, follows this inner scaling for $y^+>15$. This implies that the motions added to the flow by the nanowire actuations were interacting with the turbulence, which is expected to follow inner scaling.

One interpretation of this result is that the turbulence itself was transporting the active nanowire surface induced eddies away from the wall and across the wall layer. Since turbulent eddies typically only interact with eddies of the same scale, the energy content of the turbulent eddies produced on the same scale as the nanowire motions depends on the distance from the wall and location in the wall layer. These eddy interactions produced a non-monotonic dependence with wall-normal distance such as those seen in figures 5.7(a) and 5.7(b)

Also shown in figures 5.7(a) and 5.7(b) is the lack of collapse in the profiles for $y^+<15$. The lack of collapse in this region suggests that the efficiency of the nanowires to add kinetic energy to the flow is no longer dependent upon the turbulence levels but instead dependent upon the nanowire surface properties in relation to the flow. With increasing Reynolds numbers, the ratio of nanowire length to viscous sublayer thickness, r_w, increased, offering a possible explanation for the increase in efficiency of the nanowires to impart kinetic energy into the flow. Consequently, due to the lack of turbulence level dependence, it is also within this region, $y^+<15$, that the nanowires can be expected to have the greatest effect on altering the turbulence.

Therefore, even though nanowire surface actuation effects can be detected throughout the wall layer, it is only within the region of $y^+<15$ that these effects were driven by solely the nanowire motions. Beyond $y^+=15$, these motions were interacting with and being transported away from the surface by the turbulence itself.

5.4 Nanowire Effects

To distinguish the effects of the active nanowires from those created by the motion of the PZT disk, the nanowires were abraded from the surface of the 12.7 mm PZT disk and the experiment repeated at Re_τ=2400. Note that care was taken to ensure the PZT surface remained flush with the tunnel wall after abrasion as in previous experiments.

A comparison between the frequency spectra of the surface before and after nanowire abrasion, shown figures 5.8(a) and 5.8(b), display the characteristic peak at the actuation frequency for both nanowire-covered and bare PZT cases. Although the peak is present in the spectrum after nanowire abrasion, the peak from the surface containing nanowires is considerably larger in magnitude showing a measurable addition of kinetic energy from the nanowires, in contrast to the bare PZT surface. The relative difference between the magnitude of these peaks is made more apparent in figure 5.8(b), showing the pre-multiplied frequency spectra of the nanowire covered and bare PZT surface. At the actuation frequency, the nanowire-laden surface injects more kinetic energy into the flow than any other frequency in the spectrum, whereas the same surface without the nanowires has negligible energy contributions.

Also apparent in these graphs is the secondary peak at $2f_{act}$ which drops to noise levels when the nanowires have been removed. Given the characteristics of a hot-wire probe's response to transverse motions, this suggests the removal of the wires has prevented the production of shear driven transverse motions and left only the thrusting motions of the PZT wafer.

To better quantify this kinetic energy addition, figure 5.9 shows the kinetic energy addition at the actuation frequency for the nanowire containing surface and the bare PZT surface after nanowire abrasion. Utilizing the same calculations as before (see Section 5.1), the kinetic energy difference between actuated and unactuated cases

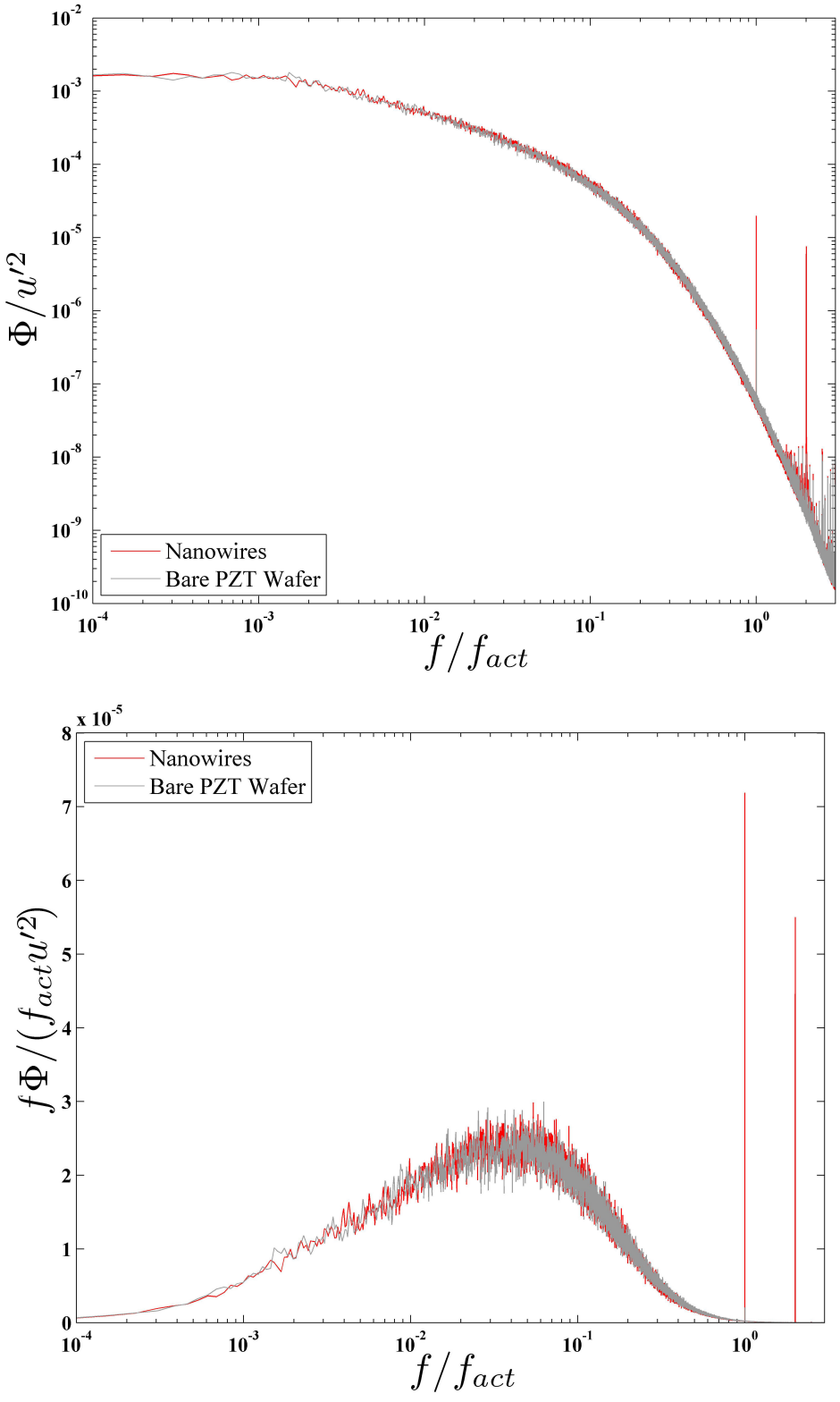

Figure 5.8: Frequency spectra of 12.7 mm diameter nanowire surface in comparison to bare PZT surface after nanowire abrasion (a) with corresponding pre-multiplied spectra (b).

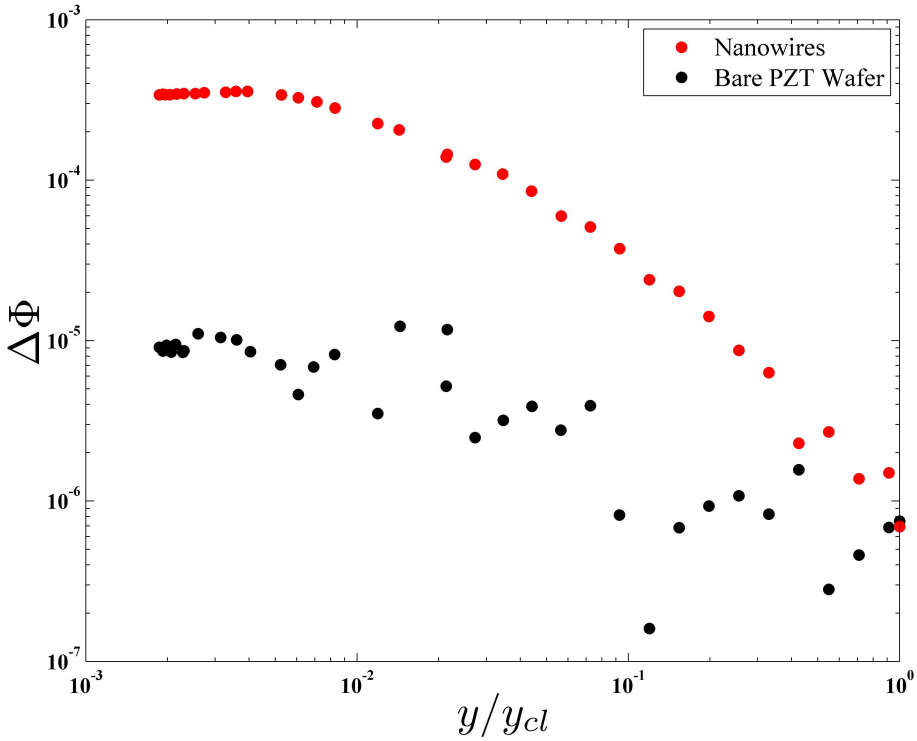

Figure 5.9: Additional kinetic energy injected into the turbulence due to nanowire surface actuation in comparison to bare PZT surface action.

shows the nanowires work to amplify this kinetic energy contribution to the flow by almost two orders of magnitude relative to the bare PZT surface.

CHAPTER 6 CONCLUSIONS AND FUTURE WORK

An experimental investigation was conducted to determine whether actuated nanowire surfaces could introduce kinetic energy into fully turbulent wall-bounded flow. To conduct this investigation, actuated nanowire surfaces were placed in fully developed, channel flow at different Reynolds numbers and the modifications to the turbulence were measured using hot-wire anemometry.

This research has shown that dynamically actuated nanowires immersed in a viscous sublayer introduce measurable motions into a turbulent flow field. Evidence of the induced motions are seen as sharply defined peaks in the spectral analysis of the velocity at the actuation frequency. This energy addition is strongly dependent on the active nanowire surface area. It is expected that larger arrays would increase the nanowire induced effects on the flow field and more clearly resolve the exact motions and influences of the active nanowires.

A second peak in the energy spectra at twice the actuation frequency was observed, which is taken as evidence that additional energy is contributed by the transverse motion of the nanowires. This suggests that rather than the pressure waves introduced by the piezoelectric disc, the actuated nanowires are imparting transverse, shear motions into the turbulent flow field as well. These transverse oscillatory motions have been shown in previous research to have strong influence in turbulence control and drag reduction. These shear driven motions and underlying sources are yet unclear.

The induced motions from the active nanowires within the viscous sublayer are transported by the turbulence into the buffer layer where the majority of turbulence

is produced. This turbulent transport was found to be Reynold's number dependent, with higher Reynold's numbers exhibiting greater kinetic energy additions.

In summary, the nanowires were found to introduce kinetic energy into the flow-field where it could have the greatest effect, however the net effect in this particular actuation scheme was negligible. These results suggest there is potential for the use of active nanowires for flow manipulation. However much work must be done before this is realizable.

Two areas can be identified for further development. It is suspected that the isotropic actuation used in the study presented here was far from optimal for modifying the buffer layer studies. Therefore, future work should be conducted investigating transversely oscillating nanowires, preferably with a traveling wave motion. In addition, the results presented here used a relatively small actuator, however they do suggest a significant improvement in the kinetic energy transported into the flow with an increase in actuation area. Therefore, a detailed study is required to investigate the required actuator dimensions necessary to introduce significant modifications into the flow.

Coupled with these parametric studies should be additional interrogations to acquire a deeper understanding of how specific nanowire motions influence bulk flow properties, for example using multi-point and/or a multi-directional hot-wire measurements, which could offer further insight into the mechanisms driving this secondary turbulent kinetic energy addition.

BIBLIOGRAPHY

[1] Bahareh Estejab. An investigation of the reynolds dependence of the near-wall peak in canonical wall bounded turbulent channel flow. Master's thesis, University of Kentucky, 2011.

[2] H. Sodano, T. M. Seigler, and C. Bailey. Near wall shear stress modification using an active piezoelectric nanowire surface. Technical report, University of Florida and University of Kentucky, 2012.

[3] Encyclopdia Britannica. *Turbulent Flow*. Encyclopdia Britannica Inc., 2013.

[4] H. W. Liepmann. The rise and fall of ideas in turbulence: Research in turbulence, still the most difficult problem of fluid mechanics, continues to produce technological advances, but the path of progress is anything but straight. *American Scientist*, 67(2):pp. 221–228, 1979.

[5] Luca Biferale. Shell models of energy cascade in turbulence. *Annual Review of Fluid Mechanics*, 35(1):441–468, 2003.

[6] A. N. Kolmogorov. The local structure of turbulence in incompressible viscous fluid for very large reynolds numbers. *Dokl. Akad. Nauk SSSR*, 30:301–305, 1941.

[7] M. V. Zagarola and A. J. Smits. Mean-flow scaling of turbulent pipe flow. *Journal of Fluid Mechanics*, 373:33–79, 10 1998.

[8] I. Marusic, B. J. McKeon, P. A. Monkewitz, H. M. Nagib, A. J. Smits, and K. R. Sreenivasan. Wall-bounded turbulent flows at high reynolds numbers: Recent advances and key issues. *Physics of Fluids*, 22(6):065103, 2010.

[9] A. J. Smits, B. J. McKeon, and I. Marusic. High-Reynolds number wall turbulence. *Annu. Rev. Fluid Mech.*, 43:353–75, 2011.

[10] C. K. Chan, H. Peng, Liu G., K McIlwrath, X. F. Zhang, R. A. huggins, and Y Cui. Hgih performance lithium battery anodes using silicon nanowires. *Nature Nanotechnology*, pages 31–35, 2008.

[11] M. Ge, J. Rong, X Fang, and C Zhou. Porous doped silicon nanowires for lithium ion battery anode with long cycle life. *Nano Letters*, 12(5):2318–2323, 2012.

[12] J. A. Czaban, D. A. Thomson, and R. R. LaPierre. Gaas coreshell nanowires for photovoltaic applications. *Nano Letters*, 9(1):148–154, 2009.

[13] Y. Dong, B. Tian, T. J. Kempa, and C. M. Lieber. Coaxial group iiinitride nanowire photovoltaics. *Nano Letters*, 9(5):2183–2187, 2009.

[14] O Muskens, J Rivas, R. Algra, E Bakkers, and A Lagendijk. Design of light scattering in nanowire materials for photovoltaic applications. *Nano Letters*, 8(9):2638–2642, 2008.

[15] Y. B. Tang, Z. H. Chen, H. S. Song, C. S. Lee, H. T. Cong, H. M. Cheng, W. J. Zhang, I. Bello, and S. T. Lee. Vertically aligned p-type single-crystalline gan nanorod arrays on n-type si for heterojunction photovoltaic cells. *Nano Letters*, 8(12):4191–4195, 2008.

[16] K. Haraguchi, T. Katsuyama, and K. Hiruma. Polarization dependence of light emitted from gaas p?n junctions in quantum wire crystals. *Journal of Applied Physics*, 75:4220, 1994.

[17] B. Piccione, C. Cho, L. K. Van Vugt, and R. Agarwal. All-optical active switching in individual semiconductor nanowires. *Nature Nanotechnology*, pages 640–645, 2012.

[18] J. Zhou, P Fei, Y. Gao, Y. Gu, J. Liu, G. Bao, and Z. L. Wang. Mechanicalelectrical triggers and sensors using piezoelectric micowires/nanowires. *Nano Letters*, 8(9):2725–2730, 2008.

[19] Y. Qin, X. Wang, and Z. L. Wang. Microfibrenanowire hybrid structure for energy scavenging. *Nature*, pages 809–813, 2008.

[20] X. Wang, J. Liu, J. Song, and Z. L. Wang. Integrated nanogenerators in biofluid. *Nano Letters*, 7(8):2475–2479, 2007.

[21] X. Wang, J. Song, J. Liu, and Z. L. Wang. Direct-current nanogenerator driven by ultrasonic waves. *Science*, 316:102–105, 2007.

[22] Zhong Lin Wang and Jinhui Song. Piezoelectric nanogenerators based on zinc oxide nanowire arrays. *Science*, 312(5771):242–246, 2006.

[23] Z. Ming, L. Jian, W. Chunxia, Z. Xiaokang, and C. Lan. Fluid drag reduction on superhydrophobic surfaces coated with carbon nanotube forests (cnts). *Soft Matter*, 7:4391–4396, 2011.

[24] C. Chen, M. Ma, K. Jin, J. Z. Liu, L. Shen, Q Zheng, and Z. Xu. Nanoscale fluid-structure interaction: Flow resistance and energy transfer between water and carbon nanotubes. *Physical Review E*, 84:046314, Oct 2011.

[25] W. J. Jung, N. Mangiavacchi, and R. Akhavan. Suppression of turbulence in wall-bounded flows by high-frequency spanwise oscillations. *Physics of Fluids A: Fluid Dynamics*, 4(8):1605–1607, 1992.

[26] H. Choi, P Moin, and J Kim. Active turbulence control for drag reduction in wall-bounded flows. *Journal of Fluid Mechanics*, 262:75–110, 9 1994.

[27] K. S. Choi and B. R. Clayton. The mechanism of turbulent drag reduction with wall oscillation. *International Journal of Heat and Fluid Flow*, 22(1):1 – 9, 2001.

[28] O. Bilgen, C. De Marqui, K. B. Kochersberger, and D. J. Inman. Macro-fiber composite actuators for flow control of a variable camber airfoil. *Journal of Intelligent Material Systems and Structures*, 22(1):81–91, 2011.

[29] F. Laadhari, L. Skandaji, and R. Morel. Turbulence reduction in a boundary layer by a local spanwise oscillating surface. *Physics of Fluids*, 6(10):3218–3220, 1994.

[30] K. S. Choi and M Graham. Drag reduction of turbulent pipe flows by circular-wall oscillation. *Physics of Fluids*, 10(1):7–9, 1998.

[31] P. Orlandi and M. Fatica. Direct simulations of turbulent flow in a pipe rotating about its axis. *Journal of Fluid Mechanics*, 343:43–72, 6 1997.

[32] M. Quadrio and S. Sibilla. Numerical simulation of turbulent flow in a pipe oscillating around its axis. *Journal of Fluid Mechanics*, 424:217–241, 11 2000.

[33] Choi K. S., J. R. DiBisschop, and B. R. Clayton. Turbulent boundary-layer control by means of spanwise-wall oscillation. *AIAA Journal*, 36(7):1157–1163, 1998.

[34] M. R. Dhanak and C. Si. On reduction of turbulent wall friction through spanwise wall oscillations. *Journal of Fluid Mechanics*, 383:175–195, 2 1999.

[35] Timothy W. Berger, John Kim, Changhoon Lee, and Junwoo Lim. Turbulent boundary layer control utilizing the lorentz force. *Physics of Fluids*, 12(3):631–649, 2000.

[36] S. A. Jacobson and Reynolds W. C. An experimental investigation towards the active control of turbulent boundary layers. Technical Report TF-64, Stanford University, 1995.

[37] R. F. Blackwelder, D. Liu, and Jeon W. P. Velocity perturbations produced by oscillating delta wing actuators in the wall region. *Experimental Thermal and Fluid Science*, 16(12):32 – 40, 1998.

[38] R. F. Blackwelder and W. P. Jeon. Perturbations in the wall region using flush mounted piezoceramic actuators. *Experiments in Fluids*, 28(6):485–496, 2000.

[39] V Kumar, M Hays, E Fernandez, W Oates, and F. S. Alvi. Flow sensitive actuators for micro-air vehicles. *Smart Materials and Structures*, 20(10):105033, 2011.

[40] J. P. Monty. *Developments in Smooth Wall Turbulent Duct Flows*. PhD thesis, University of Melbourne, 2005.

[41] S. Tavoularis. *Measurement in Fluid Mechanics*. Cambridge University Press, 2005.

[42] J. B. Barlow, W. H. Raie, and A. Pope. *Low-Speed Wind Tunnel Testing 3rd. Edn.* John Wiley & Sons, 1999.

[43] P.M. Ligrani and P. Bradshaw. Subminiature hot-wire sensors: development and use. *J. Phys. E: Sci. Instrum.*, 20:323–332, 1987.

[44] F Jorgenson. *How To Measure Turbulence with Hot-Wire Anemometers - A Practical Guide*. Dantec Dynamics, 2002.

[45] W.P. Graebel. *Engineering Fluid Mechanics*. Taylor and Francis, 2001.

Christopher was born in Lexington, KY. In 2007, he attended Bucknell University earning a B.A. majoring in Physics with a minor in Mathematics. Following, he continued his educational endeavors at the University of Kentucky pursuing an M.S. in Mechanical Engineering. There he received his Lean Systems Student Certification from the university.

Christopher R. Guskey
7/16/2013